Quantitative Assessment of the Human Inner Ear: Toward Endolymphatic Hydrops Segmentation

Fatemeh Nejatbakhshesfahani

München

Aus der Klinik und Poliklinik für Radiologie
Klinik der Ludwig-Maximilians-Universität München
Vorstand: Univ. Prof. Dr. Jens Ricke-Laville

Quantitative Assessment of the Human Inner Ear: Toward Endolymphatic Hydrops Segmentation

Dissertation
zum Erwerb des Doktorgrades der Humanbiologie
an der Medizinischen Fakultät
der Ludwig–Maximilians–Universität München

vorgelegt von
Fatemeh Nejatbakhshesfahani
aus Iran, Sanandaj

München, 2020

Mit Genehmigung der Medizinischen Fakultät der
Universität München

Berichterstatter: Univ. Prof. Dr. med. Birgit Ertl-Wagner

Wissenschaftliche Mitbetreuung durch: Dr. med. Valerie Kirsch

Mitberichterstatter: Prof. Dr. Friedrich Ihler

Dekan: Prof. Dr. med. dent. Dr. h.c. Reinhard Hickel

Tag der mündlichen Prüfung: 11.11.2020

تقدیم به مادرم

که به من آموخت برای هر در بسته‌ای کلیدی هست!

حتی اگر بتوانست باز باشد...

    Dedicated to my mother
who taught me that there is always a key for any closed door,
even if it could be open!

Contents

Eidesstattliche Versicherung

Ich erkläre hiermit an Eides statt, dass ich die vorliegende Dissertation mit dem Thema:

Quantitative Assessment of the Human Inner Ear: Toward Endolymphatic Hydrops Segmentation

selbständig verfasst, mich außer der angegebenen keiner weiteren Hilfsmittel bedient und alle Erkenntnisse, die aus dem Schrifttum ganz oder annähernd übernommen sind, als solche kenntlich gemacht und nach ihrer Herkunft unter Bezeichnung der Fundstelle einzeln nachgewiesen habe. Ich erkläre des Weiteren, dass die hier vorgelegte Dissertation nicht in gleicher oder in ähnlicher Form bei einer anderen Stelle zur Erlangung eines akademischen Grades eingereicht wurde.

München, den 10.11.2020
Fatemeh Nejatbakhshesfahani

List of Figures

List of Tables

Abstract

Gravity and the orientation of the body in space are vital features to monitor the surrounding environment. An intact and functioning vestibular system is an important prerequisite for orientation in space [59].The vestibular labyrinth in the inner ear consists of the semicircular canals, the otolith organs and receptors [127]. These receptors transmit vestibular information through the vestibulocochlear nerve to the cerebellum and to nuclei in the brainstem, from where information is further processed [60].

The main components of the membranous labyrinth of the inner ear is identified as the three semi-circular ducts (horizontal, anterior and posterior), two otolith organs (saccule and utricle), and the cochlea [127].

When the vestibular system is damaged by illness or injury, vestibular symptoms typically ensue. These include dizziness and balance and are often accompanied by problems with hearing or vision [61].

Menière's disease is clinically characterized by episodic vertigo, low frequency fluctuating sensorineural hearing loss, tinnitus, and a sensation of fullness on the affected side. Gait problems, postural instability, and drop attacks may accompany [62]. Endolymphatic hydrops is assumed to be the morphological hallmark feature of *Menière's* Disease [5], which could be detected by contrast-enhanced high resolution MR imaging [56] [67] [80] [81] [85] [99] [5].

The study was divided into three different phases:
In the first phase, a reliable methodology for achieving a co-registered dataset was proposed which used a nonlinear deformable registration, landmark-based registration, using bsplines. This was a part of pre-processing of the dataset and is the prerequisite for any clinical image

processing study.

The second phase aimed to extract the bony structure of the human left and right inner ears within the MRI scans. In order to achieve this aim, a novel idea for generating a probabilistic atlas for the bony labyrinth of the human inner ear was presented and published in [1]. This atlas was validated based on three different datasets and demonstrated a high agreement in regard to the performance scores. The bony structure was segmented in a reliable atlas based segmentation [1]. The establishment of this probabilistic atlas enabled us to develop a methodology for a semi-automatic segmentation based on the atlas to further investigate the concentration of different fluids inside the membranous labyrinth [1].

Methodologically, twenty-four individuals with vestibular migraine without endolymphatic hydrops were included in the study (12 females, aged 20 - 76 years, mean age: 51.5 ± 3.9 years) [1]. Additional datasets for the verification and validation phase were also included in the current study [1]. These additional datasets or unseen subjects 'data were used as testing sets with different characteristics compared to the training set in order to verify the applicability of the atlas for not only the atlas dataset subjects but other subjects diagnosed with or without hydrops.

Using CISS images generated on a 3T magnetic resonance (MR) scanner, both inner ears were cropped and registered to the initial template's common reference from [18].

Subsequently, 96 models were extracted from two manual segmentations of each subject's cochlea and vestibule and a probabilistic labeled atlas was created by a label based approach. Ultimately, the 3D inner ear atlas consisting of internal auditory meatus, cochlea, vestibule and semicircular canals for both right and left ears was obtained using a label based approach for atlas generation.

The evaluation of the atlas performance was conducted using Dice scores in three different scenarios for the variation of study population, number of fiducial markers and smoothing Gaussian kernel and the optimum value was identified for the algorithm. Since the atlas-based segmentation extracts the bony labyrinth of the human inner ear, the fluid classification within the extracted masks or volumes of

interest was straight forward. Two testing datasets were used to validate the performance of the atlas based segmentation.

The results showed the variation of volumes of the inner ear components. The Dice score was found to be 89% for the right side and 86% for the left side [1] using the optimum values for smoothing kernel: 5 voxels, number of subjects: 24 and number of control points: 5 [1]. The Dice scores showed an overestimation in certain subjects which could be remedied by a better manual segmentation of the boundaries [1]. The RMSE (root mean square error) of the control points position on a training set and two different testing sets was $3.8\% \pm 0.2$ on average for the whole sample [1]. The generated atlas showed the variation of the inner ear shape and size across individuals in the total sample.

This study for the first time proposed a three-dimensional atlas for the human inner ear. The generated atlas was applied in a semi-automatic atlas-based segmentation to obtain a mask of the CISS sequence [1]. The mask is an important achievement to monitor ELH in therapeutic trials in *Menière's* disease using contrast enhanced MR sequences.

In the third phase of the study, a multiparametric approach for image segmentation was applied based on i) an atlas-based approach for the CISS sequence, ii) supervised learning with active contours for the FLAIR sequence and iii) a subtraction technique with nonlinear interpolation for the FLAIR sequence. This resulted in the classification of ELS and PLS within the inner ear.

In summary, a statistical quantitative analysis of imaging data was established to be used in combination with qualitative symptom-based information for monitoring and grading endolymphatic hydrops. This is expected to become an essential toolbox for imaging-based studies of vestibular syndromes and also for monitoring the success of treatment strategies.

Zusammenfassung

Schwerkraft und Orientierung des Körpers im jeweiligen Raum sind essentielle Voraussetzungen für die Beobachtung der Umgebung. Das *Vestibularsystem* sorgt für diese Funktionalität [59].

Die Hauptstruktur des Vestibularsystems befindet sich im Innenohr in einem System, das als Vestibularlabyrinth bezeichnet wird. Das vestibuläre Labyrinth im Innenohr besteht aus den halbkreisförmigen Kanälen, den Otolithenorganen und den Rezeptoren [127]. Diese Rezeptoren übertragen vestibuläre Informationen über den Nervus vestibulocochlearis in das Kleinhirn und in die Kerne im Hirnstamm [60]. Die vestibulären Kerne leiten die erhaltenen Informationen an vorbestimmte Ziele weiter [60].

Das membranöse Labyrinth des Innenohrs besteht aus den drei halbkreisförmigen Kanälen (horizontal, anterior und posterior), zwei Otolithenorganen (Sacculus und Utriculus) und der Cochlea [59]. Eine Schädigung des Vestibularsystem führt in der Regel zu Schwindel und Gleichgewichtsstörungen. Auch Hör oder Sehstörungen sind häufig [61].

Morbus *Menière* ist durch episodischen Schwindel, niederfrequenten, fluktuierenden sensorineuralen Hörverlust, Tinnitus und ein Völlegefühl des betroffenen Ohres gekennzeichnet. Gangprobleme, Haltungsinstabilität und Sturzattacken können auftreten [62]. Es wird angenommen, dass ein endolymphatischer Hydrops die zugrunde liegende Pathophysiologie des Morbus *Menière* ist [5]. Ein endolymphatischer Hydrops kann mit einer kontrastmittelverstärkten hochauflösenden MRT visualisiert werden [56] [67] [80] [81] [85] [99] [5].

Die dieser Dissertation zugrundeliegende Studie wurde in drei Phasen unterteilt: In der ersten Phase wurde eine zuverlässige Methode etabliert, um einen koregistrierten Datensatz zu erhalten. Diese Meth-

ode basiert auf einer nonlinearen deformierbaren Registrierung, der Landmark-basierte Registrierung, die bsplines verwendet. Dies war ein Teil der Präprozessierung des Datensatzes und ist eine wichtige Voraussetzung jeder klinischen Bildverarbeitungsstudie.

In der zweiten Phase der Studie wurden die knöchernen Strukturen des linken und rechten Innenohrs aus MRT-Aufnahmen extrahiert. Um dieses Ziel zu erreichen, wurde eine neue Methode zur Erstellung eines probabilistischen Atlas für das knöcherne Labyrinth des menschlichen Innenohrs vorgestellt und veröffentlicht [1]. Dieser Atlas wurde anhand von drei verschiedenen Datensätzen validiert und zeigt eine hohe Übereinstimmung. Die knöchernen Strukturen wurden mit einer atlasbasierten Segmentierung segmentiert [1]. Die Erstellung dieses probabilistischen Atlases war in unserer Studie eine wichtige Voraussetzung für die Entwicklung einer halbautomatischen Segmentierungsmethodik, um die Anteile der unterschiedlichen Flüssigkeiten im membranösen Labyrinth zu quantifizieren [1].

Der ursprüngliche Datensatz bestand aus den hochauflösenden Innenohr MRTs von 24 Personen mit vestibulärer Migräne ohne Zeichen eines endolymphatischen Hydrops (12 Frauen; Durchschnittsalter 51.5 ± 3.9 Jahre, Altersspanne 20 bis 76 Jahre) [1]. Dieser Datensatz wurde in der Verifizierungs und Validierungsphase durch weitere Datensätze ergänzt [1]. Diese zusätzlichen Datensätze oder Daten unsichtbarer Probanden wurden als Testsätze mit anderen Merkmalen als die Trainingssätze verwendet, um die Anwendbarkeit des Atlas nicht nur für die Probanden des Atlas-Datensatzes, sondern auch für andere mit oder ohne Hydrops diagnostizierte Probanden zu überprüfen.

Es wurden CISS-Sequenzen verwendet, die in einem 3T-Magnetresonanz-Tomographen (MRT) akquiriert wurden. Diese wurden zugeschnitten, um jeweils das rechte bzw. linke Innenohr abzubilden und anschließend auf das urpsrüngliche Template registriert [18].

Anschließend wurden 96 Modelle aus zweimaligen manuellen Segmentierungen der Cochlea und des Vestibulums jedes Probanden extrahiert. Zudem wurde durch einen label-basierten Ansatz ein probabilistisch gekennzeichneter Atlas gemäß der Methode des "best selected set of models" erstellt. Mit Hilfe von einem label-basierten Ansatz zur Atlaserstellung beinhaltete der 3D-Innenohratlas schließlich

den Meatus acusticus internus, die Cochlea, das Vestibulum und der halbkreisförmige Kanal für das rechte und linke Ohr.

Die Performance des Atlas wurde mittels Dice Scores in drei verschiedenen Szenarien evaluiert und der optimale Wert für den Algorithmus identifiziert. Diese drei Szenarien waren eine Variation der Studienpopulation, der Anzahl der Kontrollpunkte und die Glättung des Gaussian Kerns.

Um die Performance der atlasbasierten Segmentierung zu validieren, wurden zwei Testdatensätze verwendet [1]. Da die atlasbasierte Segmentierung das knöcherne Labyrinth des menschlichen Innenohrs extrahiert, ist die Klassifizierung der FlÜssigkeiten innerhalb der extrahierten Maske oder des Volumens danach vergleichsweise unkompliziert.

Die Ergebnisse zeigten eine Variation des Volumens der Innenohrkomponenten [1]. Der Dice Score war 89% für das rechte Innenohr und 86% für das linke Innenohr. Dabei kamen die optimalen Werte für das Glätten des Kerns zur Anwendung: 5 Voxel und 5 Kontrollpunkte bei einer Anzahl an Probanden von 24. Der Dice Score zeigte bei einigen Probanden eine Überschätzung, welche durch eine bessere manuelle Segmentierung in den Grenzbereichen behoben werden konnte [1]. Der RMSE (root mean square error) der Kontrollpunktpositionen bei einem Trainingsdatensatz und zwei unterschiedlichen Testdatensätzen lag bei $3.8\% \pm 0.2\%$ für alle Probanden [1]. Der erzeugte Atlas zeigte die Variation der Innenohrform und größe zwischen Individuen in der Gesamtpopulation [1].

Unsere Studie hat erstmals einen dreidimensionalen Atlas des menschlichen Innenohrs für eine semiautomatische, atlasbasierte Segmentierung etabliert [1]. Durch diese semiautomatische, stlasbasierte Segmentierung konnte eine Maske in der CISS Sequenz generiert werden. Diese Maske erleichtert die Quantifizierung con Endolymphe und Perilymphe in der Diagnostik und Verlaufsbeobachtung von Patienten mit Morbus *Menière*.

In der dritten Phase der Arbeit wurde ein multiparametrischer Ansatz zur Bildsegmentierung entwickelt, der auf mehreren MRT-Sequenzen beruhte. Dieser Ansatz basierte auf: i) einem atlas-basierten Ansatz für die CISS-Sequenz, ii) einem Supervised Learning Ansatz mit ak-

tiven Konturen für die FLAIR-Sequenz und iii) einer Subtraktionstechnik mit nonlinearer Interpolation für die Kombination aus FLAIR-Sequenz und CISS-Sequenz.

Diese Methodik erlaubte die Klassifizierung von ELS und PLS im Innenohr. Die statistisch-quantitative Analyse in Kombination mit qualitativen symptombasierten Informationen ist eine wichtige Grundlage zur Diagnostik eines endolymphatischen Hydrops, aber auch zur Verlaufskontrolle im Rahmen klinischer Studien.

Chapter 1

Introduction

In this chapter, the underlying idea of this dissertation as well as the various methodological approaches are introduced. Image processing is a vital tool for many clinical application. This study focuses on the segmentation of the components of the inner ear and specifically on the evaluation of the endolymphatic space with the overarching aim of facilitating the diagnosis of endolymphatic hydrops.

1.1   Endolymphatic Hydrops

Endolymphatic hydrops (ELH) is considered to be a disorder of the vestibular system [3] [49] leading to several inner ear disorders such as vertigo, hearing loss and tinnitus which included about 0.2-0.5 % of the general population [62] [68] [58] [3] [10].

Figure 1.1 demonstrates the physiological structure of the inner ear, while figure 1.2 displays the components of the endolypmphatic fluid in green and the perilymphatic fluid in blue.

In ELH the endolymphatic space becomes augmented and the membranes can become bloated [66] by the additional endolymph concentration [66]. The comparison between a normal healthy inner ear in one hand, and in the other hand, the inner ear of a patient diagnosed with *Menière's* disease [66] is shown in figure 1.3.
Endolymphatic fluid takes plays an important part in the balance and the sensory cells of the hearing system in the inner ear [129]. Sound waves entering the ear is are forwarded to the inner ear via the tympanic membrane and middle ear ossicles and it generates fluid waves
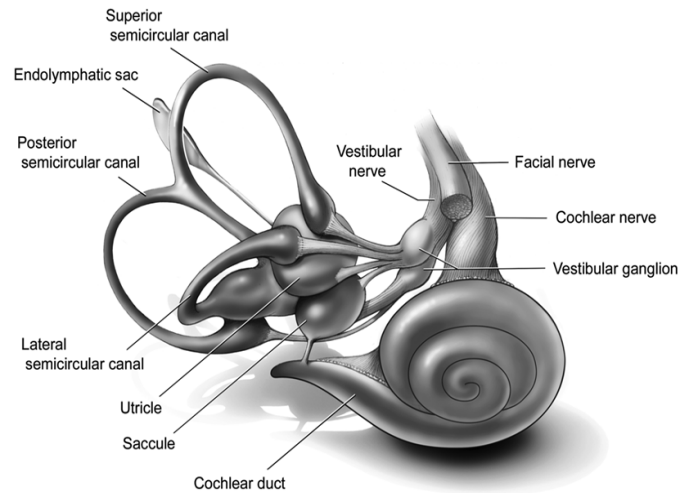
Figure 1.1: *The vestibular System and anatomy of the inner ear [61].*

in the inner ear [128]. The movement which is caused by these fluid waves in the endolymphatic fluid, stimulates the receptor cells and leads to the translation of the mechanical waves to electrical impulses [130].

Orientation of the head in the the three-dimensional space entails the angular acceleration of the endolymphatic fluid in the three semicircular canals of both inner ears, which stimulates the sensory hair cells called as vestibular receptors of the endolymph [130]. Again, there is a translation of mechanical waves to electrical impulses and these electrical impulses are transmitted to the brain [65].

Endolymphatic hydrops causes an increased hydraulic pressure within the inner ear endolymphatic system and this surplus endolymph pressure can impact both hearing and balance [66]. Endolymphatic hydrops is a hallmark finding in $Meni\grave{e}re's$ disease [67]. Even though the exact pahthophysiologic processes are incompletely understood, characteristic symptoms of $Meni\grave{e}re's$ disease include episodes of vertigo, hearing loss, tinnitus, and the feeling of aural fullness [68].

Endolymphatic hydrops has been recognized as the underlying pathophysiology and a primary histopathological finding of $Meni\grave{e}re's$ disease [4]. Several studies demonstrated endolymphatic hydrops in patients with $Meni\grave{e}re's$ disease in the in-vivo setting using contrast enhanced high resolution MRI and correlated severity of clinical symp-

toms with the degree of endoymphatic hydrops [5].
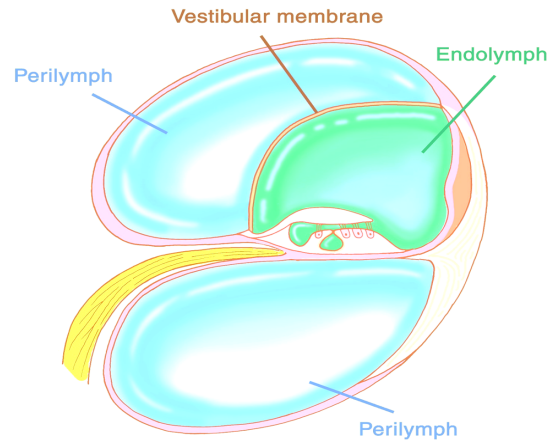
Figure 1.2: *Cross-section of a single cochlear turn, structure of organ of Corti. The scala media, filled with endolymph and surrounded by the reticular lamina is shown in green. The scala vestibule, filled with perilymph, is shown in blue [63].*
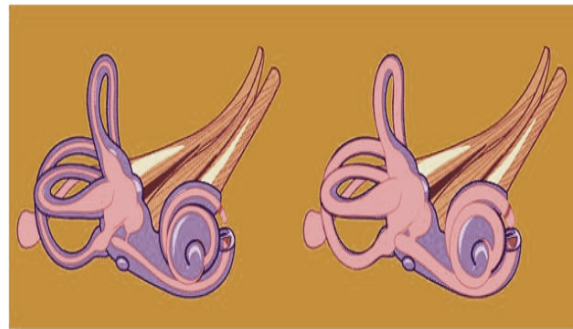
Figure 1.3: *Comparison of a visualization of the inner ear of a normal healthy ear (left) and a subject with Menière's disease (right) [64] [66]*

1.2 Computer Aided Methods for Inner Ear Segmentation

Newer contrast-enhanced, high spatial resolution MRI methods have enabled the in vivo diagnosis of endolymphatic hydrops[6]-[15].
Critical elements influencing image quality are contrast-to-noise ratio and spatial resolution of magnetic resonance images [138]. Using higher field strengths and a high number of coil elements facilitates acquiring images with a high spatial resolution and adequate signal-

to-noise ratios within acceptable scan times [138].

Endolymphatic hydrops is visualized with contrast-enhanced techniques after the administration of Gadolinium-based contrast agents (GBCA) [6]-[15]. Using these methods, perilymphatic fluid demonstrates a contrast enhancement and hyperintense signal, while endolymphatic fluid is hypointense and does not enhance.

Among the MR sequences usually acquired to diagnose endolymphatic hydrops are three-dimensional Inversion Recovery (3D-IR) sequences, three-dimensional Constructive Interface in Steady State (3D-CISS) sequences, as well as Fluid Attenuated Inversion Recovery (FLAIR) sequences [7] [9] [137] [8] [75] [134] [135], all of which are applied in a contrast-enhanced technique. These methods are usually performed on a 3 Tesla MRI scanner with a high number of coil channels [138]. Figure 1.4 shows an image acquired 24 hours after transtympanic injection of a GBCA; in this instance, a regular head coil and a surface loop coil were used in combination [138]. In recent years, intravenous administrations of GBCA are usually employed with a delayed image acquisition 4 hours after administration.

1.3   Atlas-Based Segmentation

Among automatic segmentation algorithms, atlas-based approaches have been of particular importance since they label a desired single anatomy or several anatomies from the images generated by different modalities of the medical imaging methods [16].

An atlas is interpreted as the combined information of an intensity-based image and its segmented-labeled image. These images are called templates and *atlas labels* respectively [17].

After the alignment procedure of the atlas template to the target image, the propagation of atlas labels are to the target image is resulted [17].

The principal step in every atlas creation approach is to provide a co-registered set of data which is also a basic challenge in medical image processing. Probabilistic atlases are known as a strategy in research aiming to produce anatomical templates that represent quantitative
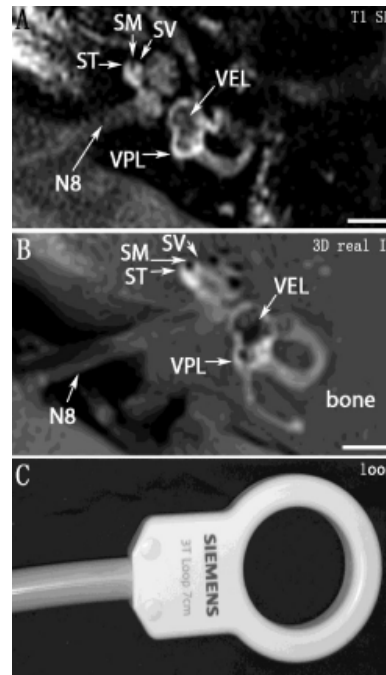
Figure 1.4: *Three Tesla MR imaging with a hybrid of a 16 channel head coil and an ear surface coil (loop 7 cm) after intra-tympanic administration of Gd-DOTA [138] in a patient with left ear Menière's disease. A: T1-weighted Spin Echo, B: 3D real IR. C: An additional loop coil was utilized. N8: 8th cranial Nerve; SM: Scala Media; ST: Scala Tympani; SV: Scalavestibuli; VEL: Vestibular Endolymph; VPL: Vestibular Perilymph. Scale bar = 5 mm [138].*

local information structural variations. As more subjects are added to the data-set for an atlas creation, it becomes more delineative than conventional atlases without miscellaneous information.

Figure 1.5 demonstrates a simple workflow for general atlas-based segmentation for human bones [55]. Different approaches to create probabilistic atlases are divided into three basic categories where the major difference is focused on the modeling method of the statistical distribution as outlined below.

1.3.1 Density-Based or Average-Intensity Approach

A density-based approach averages signal intensities of multiple MRI scans [44], [47]. For a brain atlas, MRI scans are transformable to each other using a linear or affine registration [44], [47]. Then, the intensities are normalized and averaged based on voxels which leads to generating a probability map [44], [47]. The probability maps represent the chances of finding the region of interest at a certain location
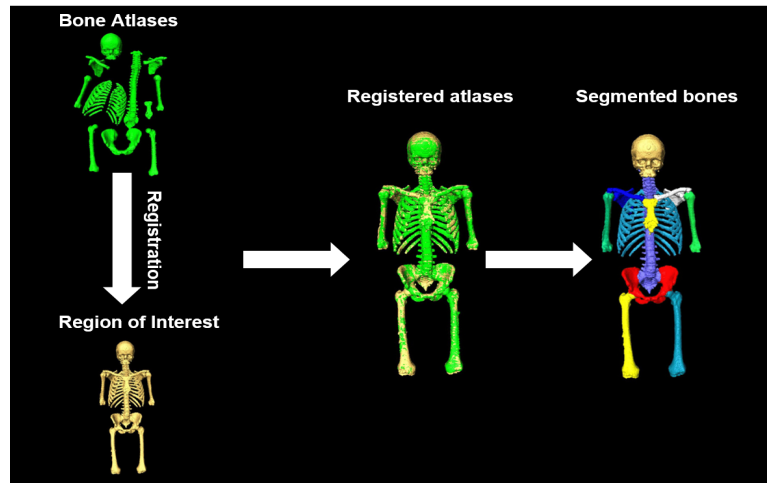
Figure 1.5: *A simple pipeline for atlas-based segmentation for human bones. The registration uses a deformable transformation approach of bone atlas to the human bone [55].*

in the atlas for a subject that has been aligned to the atlas space [44], [47].

1.3.2 Label-Based Approach

In a label-based approach, a large amount of data is manually segmented into different labels after initially aligning the subjects' data into a common reference [47], [43], [45], [44]. The quality of the manual segmentations has a pronounced impact on the generated atlas. Therefore, this step is of crucial importance in this approach. The segmentation produces a labeled image for the structure which defines the atlas. A probability map using this prior knowledge is produced for each particularized structure. This procedure is performed by using each voxel's position in three-dimensional space and characterizing the proportion of subjects assigned a selective anatomic label at this position [47], [43], [45], [44]. This is also known as a SPAM approach, an acronym for Statistical-Probabilistic Anatomy Maps. Some label based approaches apply an alignment and registration phase and produce an atlas by constructing a mean image, which should be as unbiased as possible with respect to the image dataset,. Subsequently, mean segmentations are computed from the individual segmentations [47], [43], [45], [44].

1.3.3 Deformation-Based Approaches

Using a nonlinear deformable registration method, a deformable transformation map provides information regarding the 3-dimensional patterns of anatomic differences between two subjects during the registration process [44]. This local discrepancy expression is applied further to obtain the severity of structural divergence compared the normal range, which is considered abnormality [44].

In order to include more comprehensive information in an atlas, it is always recommended to include more data subjects in the atlas generating set, since one single sample may not be appropriate representative of the whole data-set population; moreover, this approach may not contain sufficient information on variability, and therefore may not be able to judge whether a deformed structure is an admissible shape [44], [42]. One alternative to obtain model anatomical changeableness is the application of a probabilistic atlas [44], while the atlas appears as the spatial distribution of probability of belonging one pixel to a specific item [42].

Construction of a probabilistic atlas of a human anatomical organ provides information on how the structure of its mentioned anatomy varies in large populations [44]. This atlas contains data from all subjects used for its production and could assist the algorithms to identify clinically relevant structural and pattern recognition in entire populations [44], [48]. Atlases of human neuroanatomy play an important role in the visualization, detection and segmentation of various structures [47] [44].

1.4 A Review of Current Approaches

There are several previous studies on quantifying the fluid spaces of the inner ear, including the endolymphatic and perilymphatic spaces, in the literature. Several of these studies only presented visualization techniques, while some more recent publications focused on structural and characteristic analysis of the human inner ear.

Initial approaches have usually been hampered by a limited amount of data, limited image quality and limited postprocessing techniques. Recent advanced in image acquisition methodology (including higher spatial resolution and inner ear enhancement techniques) have enabled the application of novel postprocessing techniques, including methods of artificial intelligence.

1.4.1 Data Visualization and Detection

As outlined in chapter 1, recent advances in sequence technology, contrast enhancement techniques and spatial resolution have led to the in-vivo visualization of the endolymphatic and perilymphatic spaces of the human inner ear [6]-[15] [135] [136] [53] [80] [81].
Using various contrast-enhanced MRI methods, the perilymphatic space could be visualized as a hyperintense, contrast-enhancing volume, while the endolymphatic fluid is seen as a non-enhancing hypointense volume [76] [13] [52] [14]. An enlargement of the endolymphatic fluid space has been shown to correspond to a subject's recorded clinical pathology [58] [67] [77].
Several MR sequences have been described in the literature to visualize and differentiate the fluid spaces of the inner ear. These include 3D- and 2D real Inversion Recovery (IR) sequences, 3D-Constructive Interference in Steady State (CISS) sequences and Fluid Attenuated Inversion Recovery (FLAIR) sequences (figure 2.1 and 2.2) after intratympanic or delayed intravenous administration of Gadolinium-based contrast agents [7] [9]. MR imaging had been performed at field strengths of 1.5T and 3T [8] [7], but an acquisition has the advantage of achieving a higher spatial resolution when using comparable scan times.
The 3D constructive interference in steady state (3D CISS) sequence is a heavily T2-weighted, fully refocused gradient echo MR sequence [134]. Being heavily T2-weighted this sequence is well suited for imaging of structures containing fluid or surrounded by fluid [135]. CISS sequences are used to achieve a reference image of labyrinthine fluid-space anatomy. These sequences help to generate total fluid volume images [1] by visualizing the entire fluid within the whole

bony structures within the inner ear. 3D and 2D real Inversion Recovery (IR) sequences, 3D-Constructive Interference in Steady State (CISS) sequences and Fluid Attenuated Inversion Recovery (FLAIR) sequences on the other hand allow the differentiation of endolymphatic and perilymphatic spaces in dedicated contrast-enhanced protocols. The idea of grading and segmentation of endolymphatic hydrops [10] was triggered by this volume-based contrast-enhanced visualization which provides statistical and shape-based information for further investigation in patients with *Menière's* disease and other inner ear syndromes.
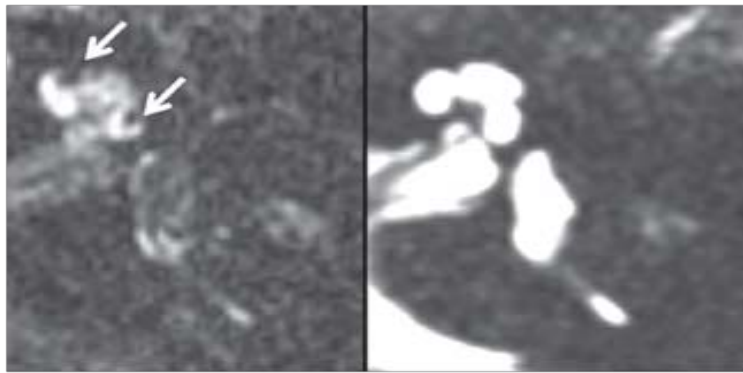
Figure 1.6: *Hydrops-positive cochlea in two dimensional FLAIR sequence (left) and CISS sequence (right). 2D-FLAIR visualizes dilated scala media of basal turn with the white arrows, ELH is visualized by low or no signal intensity region and the perilymphatic space is captured by high signal intensity regions the contrast enhancement [11].*
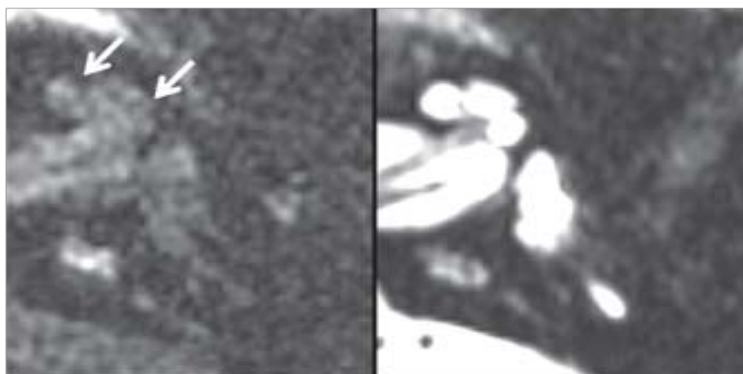
Figure 1.7: *Hydrops-negative cochlea in two dimensional FLAIR sequence (left) and CISS sequence (right). 2D-FLAIR images visualizes low signal intensity region in cochlear basal turns with white arrows [11].*

Among several methods presented to distinguish the endolymphatic

area and to highlight the difference of endolymphatic volumes in various parts of inner ear [6], some approaches entice more attention [6], [9], [10], [12].

The study conducted by [13] applies a subtraction technique (see figure 1.8) showing the perilymph signal as white, the endolymph as black, and the surrounding bone as a medium gray [6], [13], [14]. The other method presented by [7] compared the ratio of the endolymphatic space to the total summation of the endolymphatic and perilymphatic space [15].
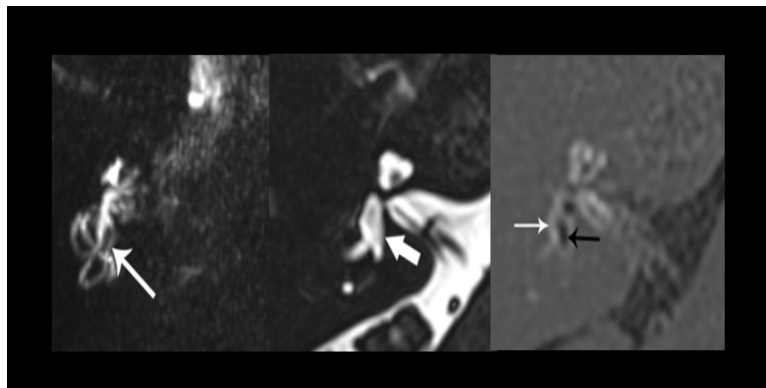
Figure 1.8: *High spatial resolution 3D-FLAIR MR imaging of a normal cochlea without endolymph hydrops. From left: Maximum intensity projection (MIP) image visualizing the hyperintense perilymph. T2 image visualizing the total lymph space. Subtracted image showing hypointense endolymph surrounded by hyperintense perilymph [56].*

Several methods have been presented to distinguish the endolymphatic space and to highlight the difference of endolymphatic volumes in various parts of inner ear [6], [9], [10], [12]. The study conducted by [13] applied a subtraction technique. Figure 2.3 shows the perilymph signal as hyperintense, the endolymph signal as hypointense [6], [13], [14]. The method presented by [7] compared the ratio of the endolymphatic space to the sum of the endolymphatic and perilymphatic spaces [15].

1.4.2 Data Representation and Segmentation

In addition to the data visualization technologies presented in section 1.4.1, there are several main approaches to differentiate structures within an image in the image processing field. Several of these

have demonstrated a higher performance and accuracy. A review of relevant publications in this field demonstrates three major methodologies, as outlined below.

Method 1

Generally, a three dimensional volume reconstruction can be performed from the two dimensional space by a slice by slice manual annotation, which is available in several image processing software [136]. Previously, the method described in [9] by Homann et al. applies the method proposed in [132] by Nawanawa et al. in which the authors succeeded to visualize the endolymphatic, perilymphatic space and bony structures after contrast agent injection [132]. The authors produced a subtraction MR cisternography from heavily T2-weighted 3D FLAIR images [132]. As shown in figure 2.4.d the perilymph demonstrates a hyperintense signal, while the endolymph is hypointense. Short and long arrows in figure 2.4 indicate enlarged cochlear endolymph and vestibular endolymph respectively [132].
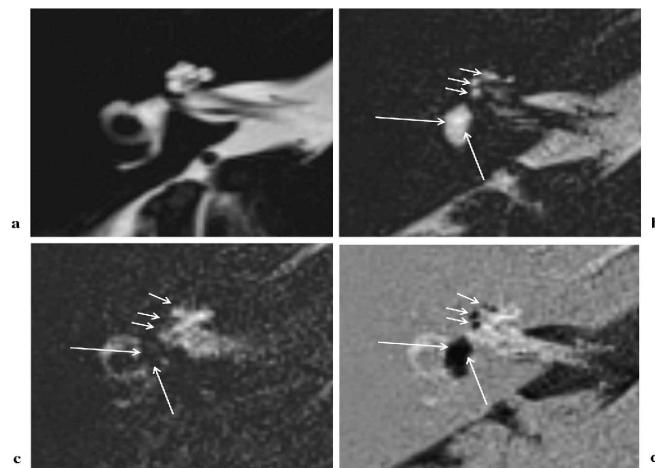
Figure 1.9: *One sample of the MRI data of a patient diagnosed with bilateral Menière's disease. A: T2-weighted CISS sequence of the right side inner ear. B: positive endolymph image acquired by a T2-weighted 3D IR sequence. C: positive perilymph image obtained by T2-weighted three dimensional FLAIR sequence. D: HYDROPS image obtained by the subtraction of the positive endolymph from the positive perilymph images [132] [7] [75] [76].*

Method 2

A study by Gürkov et al. in [10] introduced an intelligent thresholding-based segmentation in order to extract the lymph spaces of the inner ear. As the threshold is manually outlined in this method, however, the entire workflow cannot be automated. Moreover, the correlation between the intensity distribution of the surrounding area and the endolymphatic space in the FLAIR sequence limited the extendability of this method to other sequences.
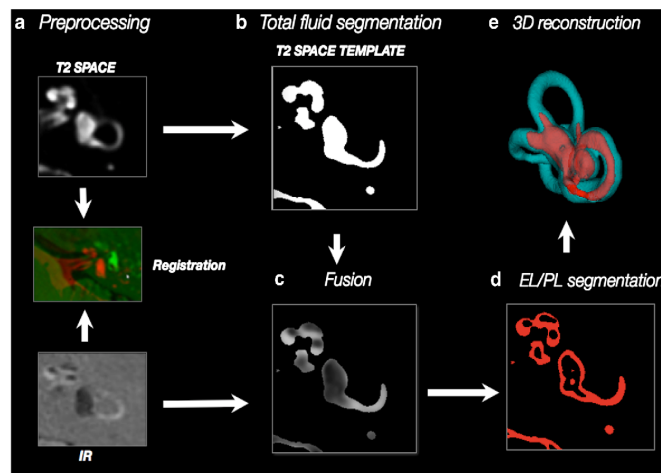
Figure 1.10: *The workflow of the EL/PL segmentation and the volumetric evaluation of the ELH [10].*

In this study sixteen patients diagnosed with definite unilateral *Menière's* disease were involved [10]. They combined CISS, T2-SPACE and IR sequences [10]. This study for the first time introduced a machine learning application for inner ear data [10]. The authors applied an automated local thresholding method for volume extraction and for the 3D reconstruction of the endolymphatic space [10]. The summarized workflow is shown in figure 2.5.

Method 3

A study published by Shanshan Zhu, Wanrong Gao, et al. [136] applied initially placed level-set contours to reconstruct a three dimensional image of the inner ear based on statistical shape models using T2-weighted MR sequences.
Figure 2.6 demonstrates a cropped region of interest which visualizes

the extraction of the total bony structure of the inner ear [136]. In their study, the authors used the level-sets to refine the initial manual segmentation of the inner ear. The resulting segmentations were visualized by the volume rendering toolbox in 3D Slicer and finally validated according to their corresponding gold standard.

In this method, an initial manual labeling is required as a prerequisite. Furthermore, the level-sets are only defined for the bony structure. Other structures are not supported in this method.
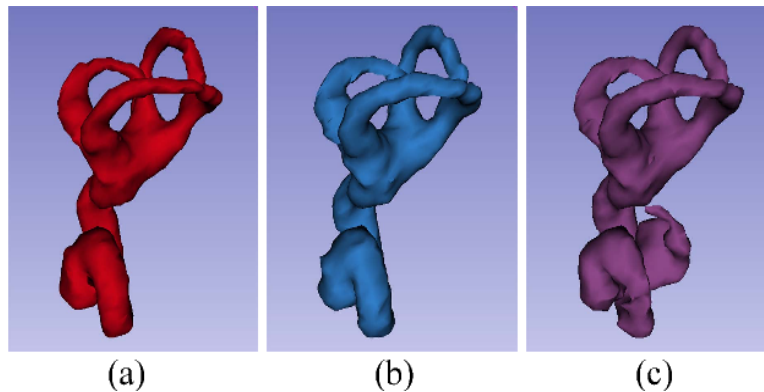
Figure 1.11: *The workflow of the 3D automatic MRI level set segmentation of inner ear based on statistical shape models [136].*

Even though the reviewed literature showed a high agreement in regard to the experts decision and accuracy, several aspects warrant further improvement:

- Time and effort needed for the assessments

- Generalization to the other sequences or modalities without manipulating the entire workflow

- Extracting target spaces in addition to bony structures

- Automation and user-independence

The studies underlying this dissertation therefore aimed to establish a new mechanism addressing the limitations in the literature.

1.5   Aim of The Dissertation

The previous publication in 2015 by [10] initiated the underlying idea for the current study. In the 2015 publication, a smart thresholding method was applied for automated local thresholding segmentation of the endolymphatic space withing the inner ear. Yet, the thresholding values change for each subject. The overarching aim of this dissertation was to create an atlas-based approach to inner ear segmentation and specifically to the segmentation of endolymphatic and perilymphatic spaces.

The research project underlying this dissertation was divided into several separate phases. In the first phase of this study, we aimed to establish a general method for analyzing any subject's data by generating a three dimensional probabilistic atlas for the human inner ear; this part is now already published as a peer-reviewed original article [1]. In this part of the dissertation, a dataset of control subjects without endolymphatic hydrops were included to produce a three-dimensional probabilistic atlas of the human inner ear.

The proposed pipeline was verified using the binary manual segmentation of the corresponding region. The atlas was applied on the MR images of different training and testing datasets for accuracy and performance measurement. The atlas-based segmentation was performed to extract the bony labyrinth of the inner ear. The segmented volume was applied as a mask on the other co-registered contrast-enhanced modalities of inner ear images.

In the second phase of the study, we aimed to establish a novel sequential multi-modal segmentation pipeline as an application of the previously published human inner ear atlas [1] as well as to extract the perilymphatic and endolymphatic spaces within the inner ear. Due to the lack of a ground truth for the validation of the second phase, ten randomly selected subjects (five control subjects without endolymphatic hydrops and five patients diagnosed with endolymphatic hydrops) were chosen and labeled by experts in consensus. The corresponding labels were used as the reference standard for the validation of the segmentation outcome.

Chapter 2

Method

In the following chapter, the workflow of the study is presented. The main methodology is divided into two subsections:
In the first section of the method chapter, data collection, pre-processing and registration, atlas generation, atlas-based segmentation, and atlas validation are covered. The target of the first part was to produce a three dimensional atlas and an updated template of the human inner ear with the supported dataset.
In the second section, an application of the generated atlas is shown and a sequential multi-modal segmentation approach for the fluid extraction inside the inner ear is proposed. Covered topics in the second part are as following: dataset, pre-processing, segmentation and validation methodology. This section was developed towards developing EL/PL atlas for the human inner ear for the future clinical application.

2.1 Human Inner Ear Probabilistic Atlas Production

The application of in-vivo, non-invasive MR imaging using intravenous contrast agent to visualize perilymphatic and endolymphatic fluid inside the human inner ear also allows of the indirect delineation of the bony labyrinth [1]. The contrast of the enhanced perilymphatic fluid to the non-enhanced endolymphatic fuid is the basis of diagnosis potential endolymphatic hydrops on imaging.
As summarized in section 1.4 currently published approaches succeeded to visualize, detect and quantify the endolymphatic and peri-

lymphatic spaces, but lacked user-interaction dependency, processing time, generalization and normalization.

Our study [1] aimed to establish the first probabilistic atlas of the inner ears bony labyrinth and to develop a workflow to extract the total endo- and perilymphatic space from different MR sequences. This workflow is considered as the initial and main step in order to obtain an automated, normalized and reproducible volumetric assessment of the endo- and perilymphatic spaces inside the bony structure of the human inner ear.

2.1.1 Requirement and Datasets

Three datasets were included and pre-processed to be used in two phases

- Phase 1: Building the probabilistic atlas

- Phase 2: Testing and Validation

Overall, 34 subjects were included in this study. This dataset was divided into three different purpose-based subsets: For the first phase, a source training dataset of MRI examination of 24 right-handed patients with vestibular migraine without endolymphatic hydrops and without measurable vestibular deficits (12 females; mean age 51.5 ± 3.9 years) [1] were included to produce the probabilistic atlas (training set: D1). Since this dataset built the atlas originally, it was used to compute the accuracy of the atlas on the training dataset in the validation section.

In the second phase, two different testing datasets (testing set 1: D2, testing set 2: D3) were examined in order to verify the generalization of the atlas for unseen subjects with or without endolymphatic hydrops. Testing set 1 (D2), contained 5 patients (3 female; mean age 48.8 ± 5.01 years) with the same characteristics as the training set [1]. Moreover, testing set 2 (D3) included five patients (one female; mean age 46 ± 5.2 years) with unilateral *Menière's* disease and endolymphatic hydrops [1]. A summary of the included datasets is provided in table 2.1. Clinical features of the included datasets are summarized in the caption of table 2.2.3.

Dataset:	Source set	Testing set I	Testing set II
Classification:	VM without ELH	VM without ELH	MM, definite unilateral ELH
min, max of age	20,76	44,61	32,60
mean std. dev of age	51.5 ±3.9	48.8 ±5.01	46 ±5.2
female gender/total	12/24	3/5	1/5

Table 2.1: Dataset information for set i: source set or training set with 24 right-handed vestibular migraine subjects without endolymphatic hydrops included to produce the probabilistic atlas, set ii: testing set I a randomly selected set of 5 unseen vestibular migraine subjects without endolymphatic hydrops for both right and left sides , set iii: testing set II a randomly selected set of 5 unseen subjects with *Menière's* disease (MD) with unilateral ELH and corresponding peripheral auditory and vestibular deficits [1].

In order to acquire the raw data, MR imaging was performed in a full-body 3 Tesla MR scanner (Magnetom Skyra, Siemens Healthineers, Erlangen, Germany [1]) which has a 20-channel head coil [1]. The scanning started with the time shift of four hours after the intravenous injection [1] (0.1 ml/kg body weight [1]) of Gadobutrol (Gadovist, Bayer, Leverkusen, Germany) [69].
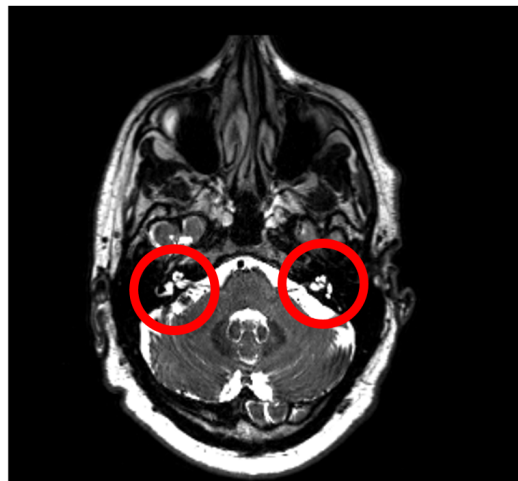
Figure 2.1: *Heavily T2weighted CISS sequence for one subject from the atlas dataset which is the training set: D1*

.

In this study, a high resolution, strongly T2-weighted, three dimensional CISS sequence of the temporal bones was selected amongst different scanned sequences in order to characterize the entire bony structure. In the figure. 2.1 an example of an image acquired with a

CISS sequence is provided. The fluid-filled inner ear's structure are markedly hyperintense and demonstrate a high contrast to the surrounding structures.

This sequence was applied to assess the bony labyrinth as the total inner ear fluid space using the parameters published in [1].

2.1.2 Pre-processing

After acquiring the raw datasets for the three separate subsets, pre-processing had to be performed for all data. The various acquired sequences have a different space alignment due to the different sequence parameters and potential motion-related misalignment. Before aligning the data, the region of interest, i.e. the inner ear structures, were cropped and extracted from the "full head scan", i.e. from the acquisition slices that covered the entire head in an axial plane. A volume of interest around the inner ear area in the CISS raw data was extracted and cropped with a three dimensional bounding box measuring 3 x 3 x 4 (cm). In figure 3.2 the VOI extraction is shown for one sample subject of our atlas production dataset [1]. In order to align the cropped
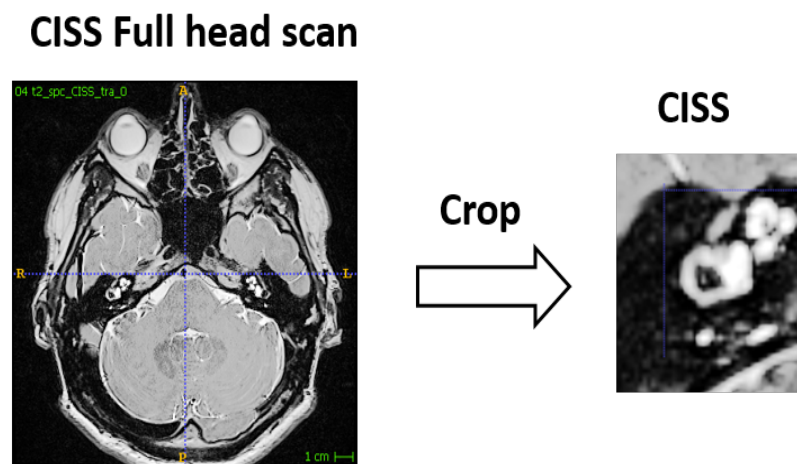
Figure 2.2: *Cropping a region of interest inside the full-head CISS sequence for one sample subject of the atlas production dataset which is the training set: D1 using a square bounding box*
.

VOIs, a source image was needed and all subjects' data were fused to achieve the source image resolution and space coordination. Initially, a template was constructed by three subjects CISS data according

to the method described in [18]. The built template was considered
as a reference and source image in the registration procedure. The
cropped VOI of the initial template's left and right side is shown in
figure. 3.3 The inner ear's structure, especially the size and shape of
the cochlea is markedly subject-dependent [19] compared to the brain
[20], therefore, using a linear or affine registration did not provide a
well-aligned registration. We compared different registration methods
on 6 randomly selected subjects and performed a two step verification
to choose the appropriate registration method for our atlas dataset.
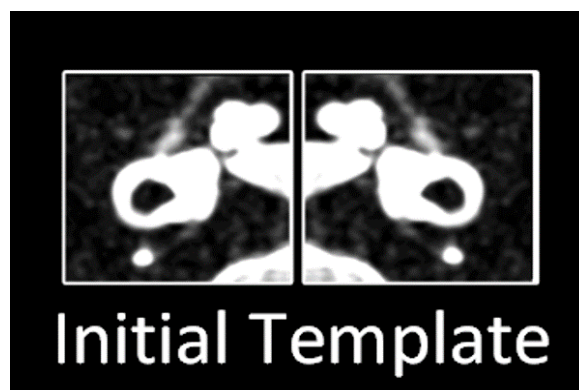
Figure 2.3: *Cropped VOI of the initial template built with three subjects' data*
.

$$Accuracy = (\frac{TruePositive}{TruePositive + TrueNegative}) \times 100 \qquad (2.1)$$

2.1.3 Nonlinear Deformable Transformation using B-splines

As mentioned, a nonlinear deformable registration method which per-
forms a reproducible pipeline is selected for the pre-processing of the
cropped volume of interest.
Taking different methods for deformable registration into account, [21]
[22] [23], the bspline deformable registration using the plastimatch
package was selected [24] [25] in slicer4.5. [26].
The deformation in the nonlinear registration method, requires plac-
ing enough fiducial markers in the three dimensional space. In this
study, the initial experiments were conducted by placing 5 landmarks
as control points.

Subsequently, it is necessary to choose the appropriate stage options in 3D slicer4.5 [26] as follows:

- *Parameter 1: Resampling Rate*: The resampling rate is offering multi-resolution alignment by cascading phases of different subsampling ratios.

- *Parameter 2: Grid Spacing*: In order to be able to control the size of the B-spline grid, this parameter is chosen. The larger grid spacing parameter corresponds to a smoother and uniformed alignment, whereas a smaller grid spacing parameter subjects to a finer registration.

- *Parameter 3: Regularization*: This parameter regularizes the problem by penalizing smoothness of the velocity field.

- *Parameter 4: Landmark Penalty*: In order to maximize the energy both on smoothness and deformation a landmark penalty is included.

- *Parameter 5: Maximum Number of Iterations*

A grid of bspline control points is built which controls the deformation of an input image. In order to compute the registration error of the moving subject versus the target image, an error measure is included. In this method, an optimization based on the quasi-Newton is applied in order to achieve the optimal alignment of the images by moving the landmarks positions and maximizing the energy on smoothness and deformation [26]. Eventually, the registered data and transformation file are exported and stored for further use in the pipeline (atlas production, atlas-based segmentation and performance measurement). In our study, the optimal stage options for Plastimatch considered during the pre-processing were detected. In this study, These options were set to: parameter 1: 1, 1, 1; parameter 2: 100; parameter 3 : 0.005; parameter 4: 10; parameter 5: 50 [1]. The detail of potential effects of non-optimal values are discussed in section 3.

Control Points

Manually placed landmarks was placed in all volumes, serving as control points during affine and deformable registration for additional

stability and accuracy. Amount of these landmarks were considered to be 15 initially. The effect of changing the number of the markers will impact the atlas performance intensively and this influence is discussed in 3.

Landmarks placement must satisfy two main features as showing distributed placements across all segmented structures in the three dimensional space, and assuring a space location that can be simply and purely detected by considering all dataset. An example of the landmarks placement distribution is presented in figure 2.4.
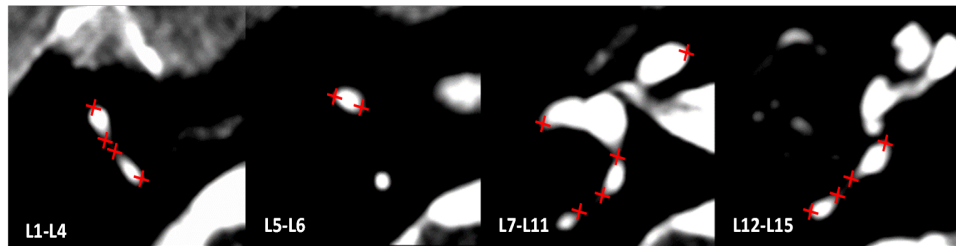
Figure 2.4: *Distribution of 15 control points in the three dimensional space for one sample subject CISS sequence*

Subsequently the data registration and pre-processing is finalized and the aforementioned nonlinear method is applied on all subjects' data. Figure. 2.5 demonstrates a registered data undergoing this workflow
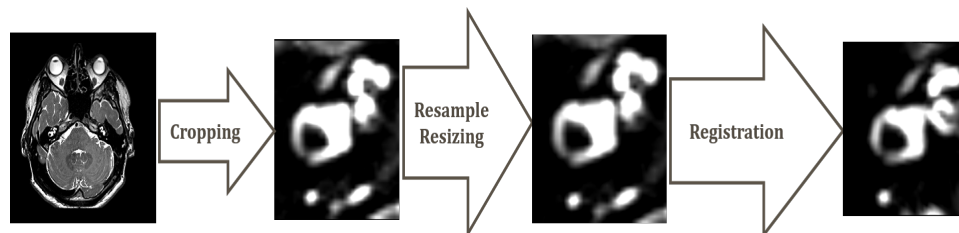
Figure 2.5: *Registered data example which underwent the cropping, resampling and resizing to the template space and registering using a deformable nonlinear transformation with bsplines*

2.1.4 Atlas Production

Several atlas generation algorithms were discussed and compared in detail in chapter 1.3. In this study, the label based approach was chosen for our inner ear atlas production. As explained in 1.3.2, we

averaged different constructed models and evaluations by experts to assure the highest performance of the label-based approach for atlas production.

In the following section the labeled model construction is described which performed an essential role in the label-based atlas production approach in our study.

Labeled Model Construction

Aiming to increase the authenticity of the final produced atlas and achieve a higher performance measure, manual segmentations were performed twice on each subject's preprocessed data.

Applying a Gaussian filter in order to smooth each segmentation to create a smoothed model is a necessary step in the pre-processing of the dataset. The direct outcome of smoothing the binary models is that the binary intensities of the edges are distributed in neighboring voxels depending on the Gaussian kernel of the filter. The Gaussian filter is usually applied for noise reduction [38]. We defined the Gaussian smoothing filter with three different kernels (σ) 3, 5 and 7 voxels in the following Gaussian filtering equation 2.1.4.

$$G(x,y) = \frac{1}{2\pi\sigma^2}e^{-\frac{x^2+y^2}{2\sigma^2}}[38] \qquad (2.2)$$

The inner ear labeled models with their corresponding data were submitted to the label-based approach for producing the probabilistic atlas for the left and right ear separately. In addition, the entire workflow was applied on the internal auditory meatus in order to separate it from the inner ear bony structure in the segmentation step. We compared the performance of the atlas using different Gaussian kernels in order to achieve the optimized value for the performance.

2.1.5   Atlas-Based Segmentation

After the inner ear probabilistic atlas for both the left and the right ear was built successfully, we proposed an atlas-based segmentation using our atlas as an application [1]. To obtain an initial segmentation for labyrinthine structures of the right and left side inner ears

of individual subjects, a thresholding based on signal intensity inside the volume of interest extracting the inner ear structures from the surrounding background was applied. These automatic threshold outlines were inspected in a slice-by-slice fashion and corrected by a trained technician [1]. The segmentations were subsequently evaluated by a neurologist with expertise in neuroimaging [1]. The final segmentation was further divided into two separated regions corresponding to

- the cochlea with three semicircular canals
- the internal auditory meatus

This regional separation was performed to create two separate atlases for the atlas-based segmentation.

In order to assign different labels to each voxel in the images of the dataset for segmentation [17] [29], we performed a image-based fusion of the template image to a objective image, which is non-linear and has the back-transformation parameters in the pre-processing step of the atlas building phase. As discussed in section 2.1.4, our three-dimensional probabilistic atlas defines two separate regions for each side in order to distinguish the internal auditory meatus from the cochlea, vestibule and semicircular canals [1]. In figure 2.6 an abstract of the entire pipeline is shown presenting the pre-processing, atlas production and performance analysis.

2.1.6 Performance Analysis

The validation of our 3D atlas of two separate regions in the human inner ear was divided into two parts. In the first part, we validated the registration approach applied on the voxels-of-interest of the subjects' data to the target image (initial template) [18]. This registration included a set of linear affine registration and nonlinear deformable transformation with bsplines. In the second part a performance analysis of the probabilistic atlas was performed. It was necessary to evaluate different aspects for the validation of atlas as several impact factors influence the performance of the atlas. The effect of these impact factors is studied in detail and the optimum values of the impact factors are determined based on the yielded performance scores.
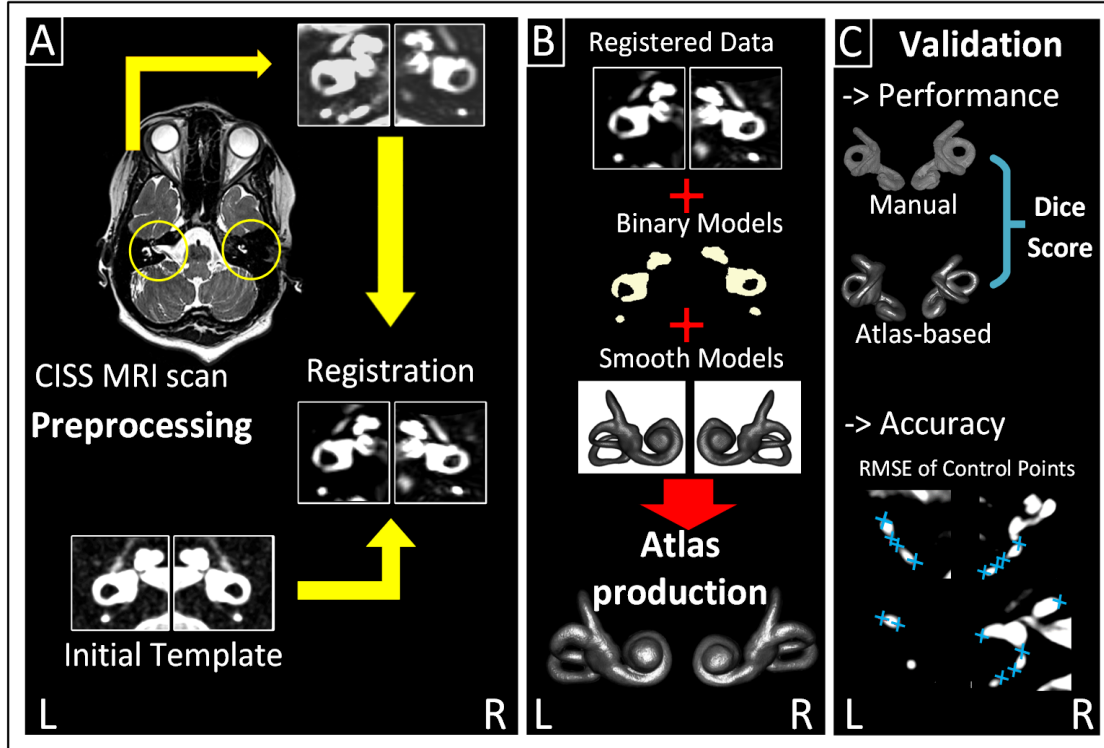
Figure 2.6: *Flowchart of the steps used to produce the probabilistic atlas of the inner ears bony labyrinths. A: Data pre-processing and alignment of the subjects CISS data to the template. During this step, the inner ear region of all subjects were cropped from the CISS MR image, resampled, and registered to a previously published initial reference template [18]. B: Atlas generation. In this step, the manually segmented label maps of each structure in the inner ear were averaged and normalized to produced a probabilistic map for every voxel. C: Validation and Performance measurement. The accuracy of the atlas-based segmentation as well as the effect of several factors on the performance score is analyzed and evaluated in this step [1].*

Registration Validation

In order to assure the reversibility of the transformation applied on the ROIs of the subjects' data, we proposed a validation methodology to ascertain that the original data was received absolutely. We therefore applied the reverse-transformation of the registration which was applied to align the data to the template. In the image space we can summarize this to: $T.X = Y \Rightarrow T^{-1}.Y = X$, in which T is the transformation matrix, X is the moving image and Y is the objective image. This equation demonstrates that applying the back-transformation on a registered image must yield to the original image space. In our study. In our study, the same concept is expanded on a set of transformations to assure the reproducibility of the original

space for the atlas-based segmentation. In order to achieve a measure for this validation, two different scores are considered. Sum of absolute difference between the voxel values in the back-transformed model and original model (SAD) is used to calculate the scientific score. Expert's binary grade which reflects the visualization overlapping and corresponds to 0 value for a wrong alignment or 1 value for the correct alignment (EBG) is used to present the clinical score. The multiplication of these two numbers as SAD.EBG if the final validation score for the reversibility of the data registration. Since this validation is only applied on the inner ear binary models, we generalized it to the whole VOI of the CISS data. In 3, the average SAD and EBG scores will be discussed in detail.
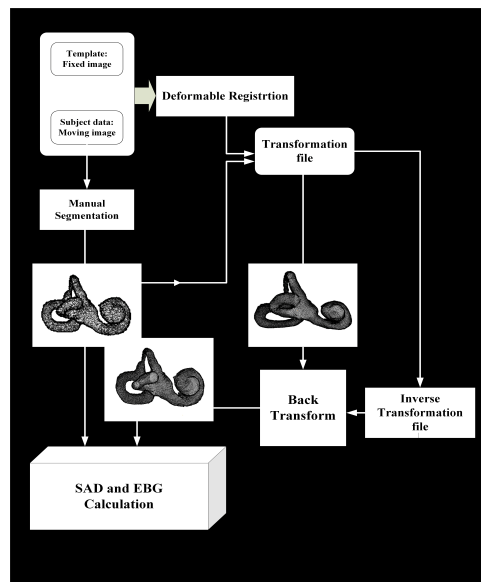
Figure 2.7: *Validation of the reversibility of the registration transformation using two different scores as sum of absolute difference (SAD) and expert's binary grade (EBG) on one sample subject's inner ear model created by manual slice-by-slice segmentation.*

Atlas-Based Segmentation Validation

The atlas-based segmentation validation, evaluates the performance of our proposed atlas in respect to the accurate extraction of the inner ear's bony structure compared to the manually segmented corresponding expert's volume. It essentially assesses not only the segmentation accuracy but the atlas performance.

Three different datasets were described in section 2.1.1 and in table 2.1. The first dataset was used for the atlas building process as the training dataset and two more dataset were used for the performance analysis as testing sets for unseen subjects. We evaluated the atlas performance on the training dataset and testing datasets. In this study, we used two different score for the atlas-based segmentation validation.

- Dice Overlap Score:
  The performance of the probabilistic atlas is evaluated by the comparison of the atlas based segmentation to a semi-manual gold-standard segmentations. A dice score [54] is defined as the main validation metric of the spatial overlap index and is calculated for the right and left inner ear structures separately. It represents the overlap and accuracy of the segmentation results. Before the dice score was calculated, the produced atlas has been thresholded by the value of 0.5 as the level of probability [1].
  The calculation of the dice score is obtained by the equation: $2 \times |X \cap Y|/|X| + |Y|$ for the voxel values in the segmentations where X is the atlas-based segmentation and Y is the gold standard ground truth as manual segmentations of the experts [1].

- Root Mean Square Error:
  Placed control points during the bspline transformation on the source image and the corresponding landmarks on the atlas-based segmented volume are employed to compute the root mean square difference for the precision evaluation. The computation is performed on three datasets including training and two testing datasets [1].

2.2 Endolymph and Perilymph Extraction with Sequential Multi-modal Segmentation

As described above, endolymphatic hydrops is visualized by the enhancement of the perilymphatic space after the administration of a Gadolinium-based contrast agent [9] [5] [13]. Fluid-attenuated inversion-recovery (FLAIR) sequences with a variable flip angle echo train are

very well suited to visualize the contrast between the enhanced peri-lymphatic space and the non-enhanced endolymphatic space [52]. Three-dimensional constructive interference in steady state (3D CISS) sequences are heavily T2-weighted fully refocused gradient echo MR sequences [51] [73] [138]. CISS sequences are used to achieve a reference images of labyrinthine fluid-space anatomy and to generate a total fluid volume images by visualizing a fully hyperintese region cor-responsing to the fluid-filled structures of the bony labyrinth [52] [53]. Several studies have focused on the detection and grading of endolym-phatic hydrops in patients with symptoms of $Meni\grave{e}re's$ disease [5] [9] [12] [10] [11] [56], thus providing semi-quantitative information besides qualitative data on symptoms [39]. Although these approaches pro-vide quantitative information in addition to visualization, they are suboptimal in regard to time efficieny and precision, as they apply manual methods and apply thresholding methods. Moreover, each method is limited to one sequence only.

As described above, we published a probabilistic atlas of the bony structure of the human inner ear based on a label-based approach [1]. In that study, we succeeded to extract the bony labyrinth from the CISS sequence in the magnetic resonance image [1]. The aim of this part of the study underlying the dissertation was to present the development of a fast and reliable method for segmentation of the endolymphatic space for future atlas of the endolymphatic system.

A three phase multimodal image segmentation pipeline was used in order to establish an approach for classification between the endolym-phatic space and the perilymphatic space. The validation was per-formed based on a thresholding method as a ground truth performed by a clinical expert. The performance analysis shows a high agreement between the ground truth and the multimodal segmentation for the endolymphatic space, yet the perilymphatic space segmentation did not include a ground truth for the purpose of validation. Therefore the perilymphatic space was extracted using a linear subtraction of the endolymphatic space from the total lymphatic space in the bony labyrinth.

A reliable semi-automatic segmentation of the endolymphatic space could play a vital role in the detection and grading of vestibular syn-

dromes and would be a requirement for endolymphatic space atlas generation in future clinical studies. For this purpose, we compared the advantages and disadvantages of potential methods for endolymphatic space and perilymphatic space segmentation, summarized in table 3.2 in section 3. We eventually chose a combination of the first and sixth method in a concept of a sequential multi-modal segmentation approach.

In figure 2.8, one sample subject's data were segmented using method 2 and method 6 mentioned in table 3.2. The PL extraction region is visualized using ITK-snap three dimensional visualisation toolbox. Our previously published three dimensional atlas [1] was an atlas-based segmentation phase was applied on top of the level sets with active contour in order to automate the VOI extraction prior to fluid classification.
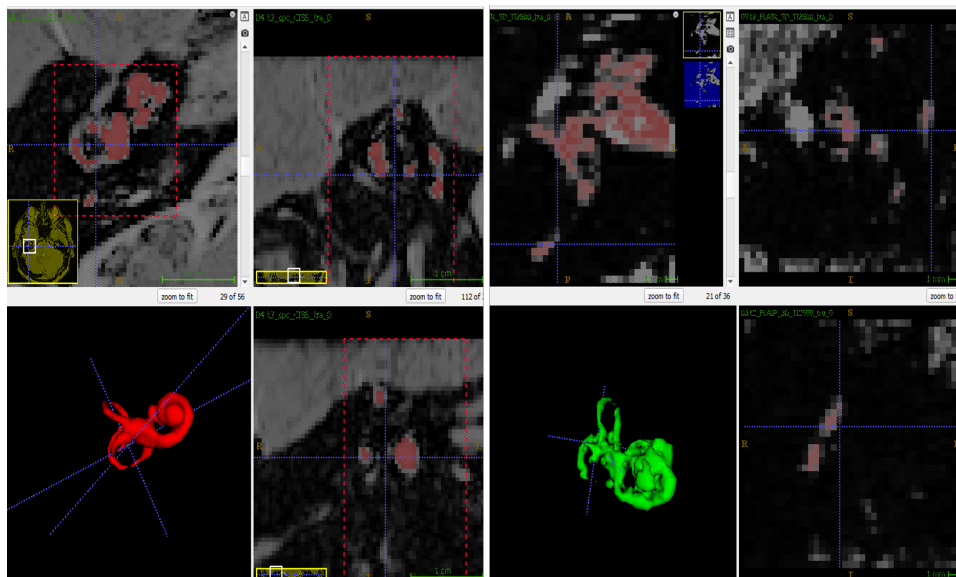
Figure 2.8: *Visualization and comparison of the results of perilymphatic space segmentation for one sample subject's data using region growing segmentation (right side green color) and level sets with active contours (left side red color)*

.

2.2.1 Dataset

In this study a dataset of twenty ears from ten subjects, was included: Five patients with bilateral endolymphatic hydrops and five control subject without endolymphatic hydrops, (5 females, 20-70 years old,

mean age: 42.5 ± 6.2 years). MR imaging data were acquired using 3 Tesla MR scanner which had the same details as explained in 2.1.1. In this section, different sequences were used based on different purposes: A 3D-FLAIR sequence to visualize endolymph from perilymph and bone separately, and a CISS sequence to lay out the total fluid space of the inner ear [1]. Image acquisition was performed in a same method as in 2.1.1 [1].

Experts in head and neck radiology and neurology performed the evaluation of the contrast-enhanced MRI and grading of the ELS [78] [1]. These experts were blinded to the clinical data of the subjective patients who were included in the study [1].

2.2.2   Pre-processing and Registration

By virtue of running a multimodal approach for image segmentation, we required an aligned registered dataset which assures all modalities are in the same space and coordination. Initially, an affine registration with resampling and resizing was performed on the FLAIR data of each subject in order to match the CISS modality space.

Additionally, a volume of interest was extracted by cropping a three dimensional box from the CISS and FLAIR sequences and a super-sampling by the value of two was applied on each CISS and FLAIR VOI. The VOI cropping matches the requirement in [1]. The same registration method, linear affine and nonlinear deformable registration using bsplines, described in section 2.1.3 was applied on the right and left side ears of CISS VOIs in order to achieve a fully aligned dataset to the template (source image). The template in this section is considered the updated template after the probabilistic atlas production algorithm since it includes more comprehensive information compared to our initial template [18].

After obtaining the suitable transformation for the CISS VOIs, the same parameters were applied on the FLAIR VOIs to transfer them to the atlas space. The pre-processing pipeline is shown in figure 2.9. The entire pre-processing of the dataset was obtained using a free and open source software for image analysis and scientific visualization, 3Dslicer [25] [26]. For the modification of the size and resolution

of the cropped VOI, ImageJ Fiji [102] was used in order to align the resolution of the reference image.
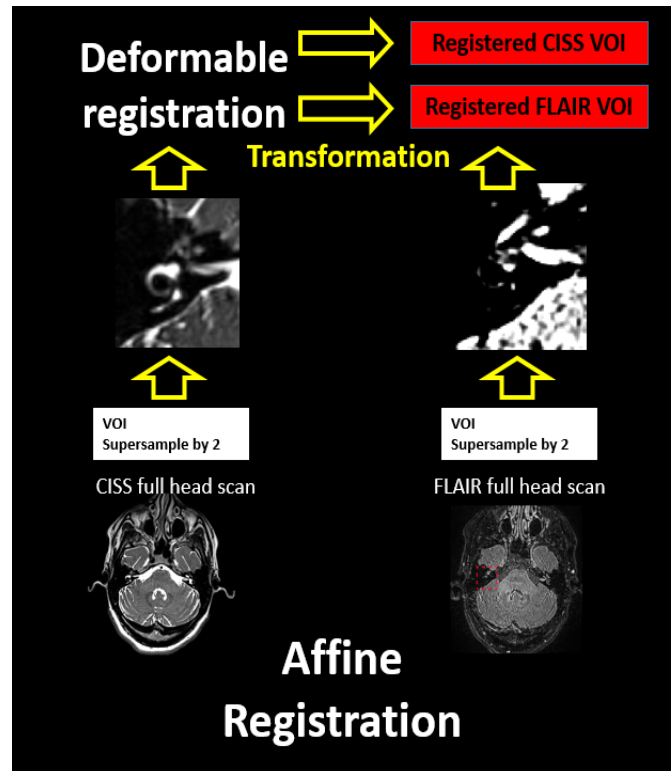
Figure 2.9: *Pre-processing of the dataset's CISS and FLAIR sequences for the EL/PL extraction using a sequential multi-modal segmentation*

.

2.2.3 Application of Machine Learning For Separating Different Lymphatic Spaces Within The Human Inner Ear

Succeeding to provide a fully aligned multi-modal dataset of left and right inner ears in the pre-processing section, the multimodal image segmentation is described in the following section, which is divided into three separate steps. These steps are illustrated in figure 2.10. This method is a combination of an atlas-based segmentation and a supervised learning approach. Since the pipeline is a step-by-step systematized sequential procedure, the segmentation approach is called a sequential multi-modal structure for image segmentation. The three major steps of this structure were as following:

- i: The CISS data provides a high resolution of the bony structure
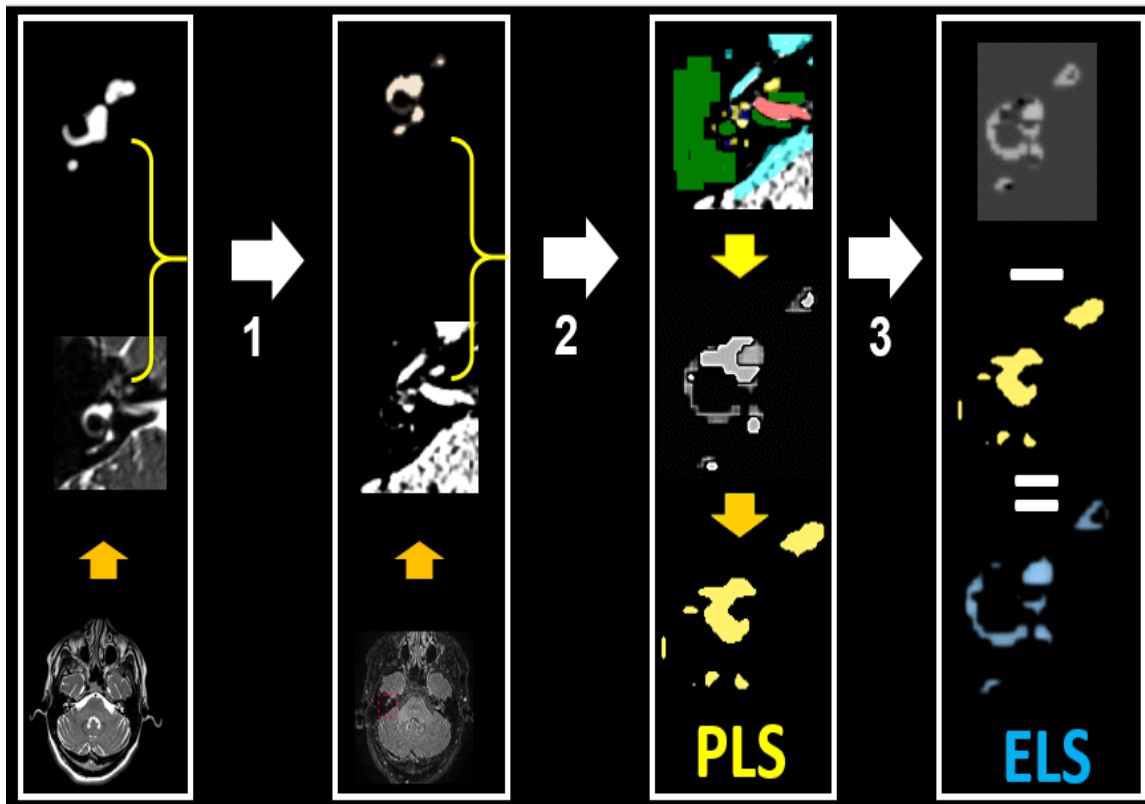
Figure 2.10: *The workflow of sequential multi-modal segmentation for EL/PL extraction within the human inner ear: 1) Atlas-based segmentation [2] of a CISS sequence for the total lymphatic space segmentation, 2) Supervised learning using levelsets with active contours for a FLAIR image for PLS segmentation and 3) subtraction technique with a nonlinear interpolation method for ELS segmentation [56].*

of the human inner ears. In the first step an atlas-based segmentation was applied on the CISS VOIs of all 20 inner ears using the published atlas [1] from our previous study. In the first step, the total lymphatic space in the preprocessed CISS sequence was extracted as visualized in figure 2.11. This volume is called TLS: total lymphatic space. The transformation parameters were applied on the atlas through the registration in the pre-processing (compare figure 2.9) to extract the TLS from the CISS data and map the corresponding regions in the target image.

- ii: The FLAIR sequence plays an important role in the fluid segmentation since it visualizes the endolymphatic fluid as a a markedly hypointense space compared to the adjacent hyperintense, contrast-enhancing perilymphatic space. In the second

step, a supervised learning using levelsets with active contours was applied on the FLAIR VOIs and the extracted bony structure on CISS. In this study ITKsnap [139] multimodal segmentation toolbox is used as: random forest with 30 trees and 25 tree depth for the training. The segmentation in i plays a mask role in order to extract the whole TLS within the FLAIR data. The result is the binary segmentation of the perilymphatic space as one class and surrounding structure within the inner ear as a second class which is shown in figure 2.12.

- iii: In order to extract the ELS in the third step, a subtraction technique is used, in which the ELS is the result of subtracting TLS segmentation in i from PLS segmentation in ii [140]. The ELS segmentation of one sample subject is visualized in figure 2.13. In this study a nonlinear interpolation for the subtraction of the volumes is considered for higher performance score. The ELS result is shown in figure 2.10 as a blue label color and the PLS result as a yellow label color.
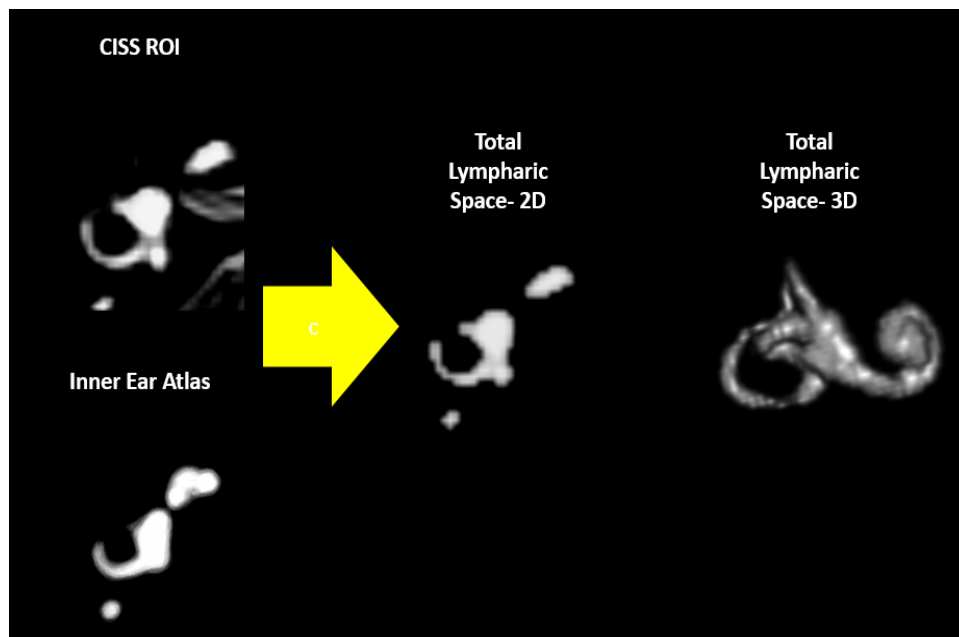
Figure 2.11: *Total lymphatic space segmentation of the CISS VOI using atlas-based segmentation with our previously published atlas [1] and its 3D visualization*
.

Consequently, all extracted ELS and PLS from left and right sides
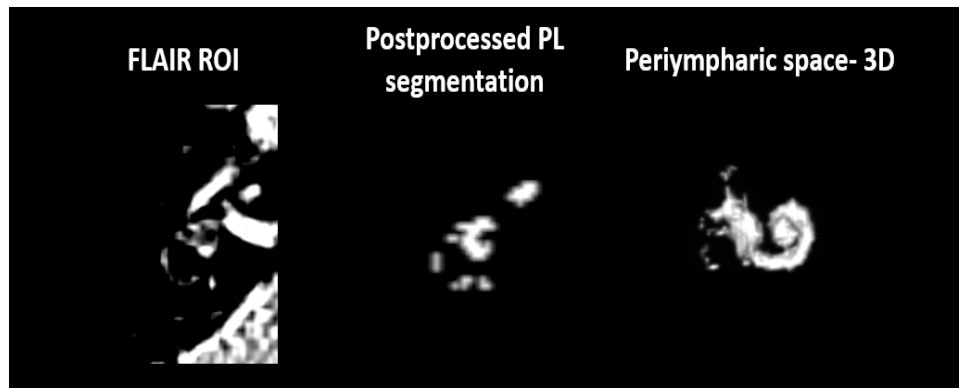
Figure 2.12: *Perilymphatic space segmentation of the FLAIR VOI using levelsets with active contours [139] in ITK snap and its 3D visualization*

.
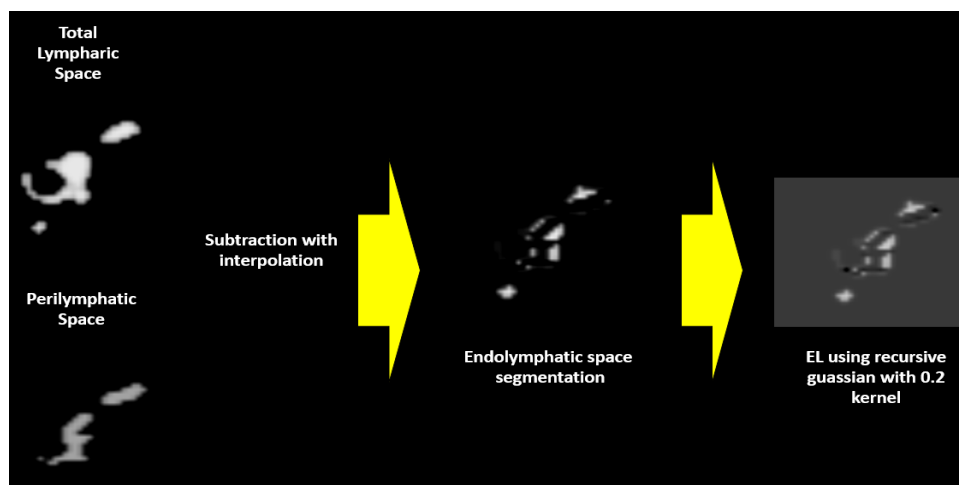
Figure 2.13: *Endolymphatic space segmentation of the inner ear using a subtraction technique with nonlinear interpolation (middle) and postprocessing (right)*

.

were collected for subjects with endolymphatic hydrops and for subjects without endolymphatic hydrops in our former dataset for performance analysis and qualitative evaluations.

2.2.4 Performance Analysis

In order to validate the results acquired with the methodology described in section 2.2.3, a performance analysis was carried out. Each segmentation step required a separate validation since these produce different structures.

For the first step of the performance analysis, a dice score [54] was

calculated to verify the atlas-based segmentation performance compared to the manual gold standard (GS1). This validation score was used previously in section 2.1.6.

For the second step, the ground truth was obtained by an interactive expert based thresholding segmentation (GS2). Finally, as the third step performance analysis, for ELS segmentation verification, the reference standard is created by the linear subtraction of GS1 and GS2, which will define the indirect endolymphatic space reference standard (GS3).

The performance score was separately calculated for the right and left sides. In addition, the dice score calculation is separated for two different subsets of the entire dataset in order to present an implicit comparison of the ELS and PLS of the healthy controls and patients with endolymphatic hydrops.

Chapter 3

Results

In this chapter, the final results of the produced probabilistic atlas, inner ear bony structure segmentation, total lymphatic space, endolymphatic space and perilymphatic space extraction are demonstrated and an example based tutorial is illustrated as a hands-on practice. In addition, quantitative measurements of the performance evaluation are described.

3.1 Method Requirements

Table 3.1, demonstrates that a deformable registration method provided high accuracy and matched well with the experts' observation scores. The accuracy score in section 3.3 is obtained by comparing the transformed manual segmentation of each subjects inner ear's bony structure and the manual segmentation of the template's bony structure.

Method	Average expert's observation score	Average accuracy score
Linear	0%	0.09%
Affine	$20\% \pm 2\%$	$32\% \pm 5\%$
Deformable	$96\% \pm 1\%$	$97\% \pm 1\%$

Table 3.1: The registration performance for six randomly selected subjects from the training dataset by applying three different registration method on each of six subjects manual segmentation of the bony structure of the inner ear and the corresponding volume in the initial template [18]

In figure 3.1, the effect of increasing the kernel size from 3 to 5 and 7 voxels for one sample subject's manual segmentation inner ear model is shown and higher kernel size leads to a smoother model. This model is extracted from the pre-processed CISS data.
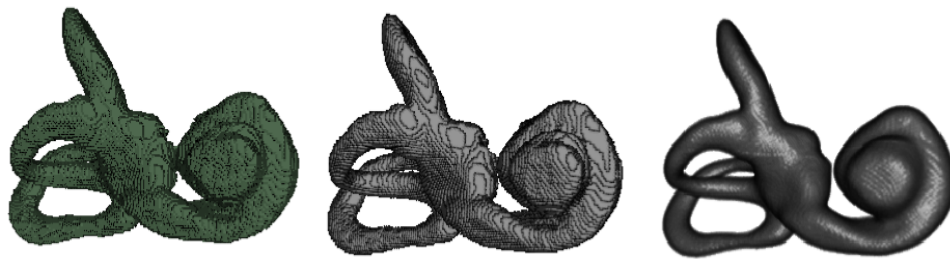
Figure 3.1: *Increasing the Gaussian kernel from 3 (left) to 5 (middle) and 7 (right) by applying a Gaussian smoothing filter on one subject's inner ear model*

The performance of different methods, atlas-based segmentation, region growing segmentation, thresholding-based segmentation, supervised learning, unsupervised learning and level-sets with active contours together with atlas-based segmentation, is summarized in table 3.2. The results showed a high performance score for our presented methodology in this study.

Method	Advantages	Disadvantages
1- Atlas based Segmentation on FLAIR	Easy and automatic and fast	Not accurate on FLAIR
2- Region Growing Segmentation	Easy to perform	Not accurate (mixed intensities) and slow
3- Thresholding Based Segmentation	Easy to perform	Not accurate
4- Supervised Learning	Accurate on FLAIR	Needs training set
5- Unsupervised Learning	Challenging, no training output needed, fast, stable	User dependent
6- Level set with active contour and atlas	Unsupervised, probabilistic model on borders, accurate, multi class result	User dependent

Table 3.2: Comparison between different potential methods for EL/PL segmentation in the human inner ear

3.2 The Three Dimensional Probabilistic Atlas of The Human Inner Ear

A three-dimensional probabilistic atlas representation is demonstrated ,as well as a three-slice-view, for the semi circular canals, cochlea and vestibule, in addition , for the internal auditory meatus in figure 4.1. Using different labels, anatomies of the inner ear, cochlea, vestibule

and semicircular canals were separated. These distinct models lead to an apportioned quantification of the lymphatic space in separated segments of the human inner ear. With assistance of image visualization software [139] [141] and [142], multiple two dimensional and three dimensional views of our human inner ear atlas are provided in figures 4.3 and 4.2 respectively.
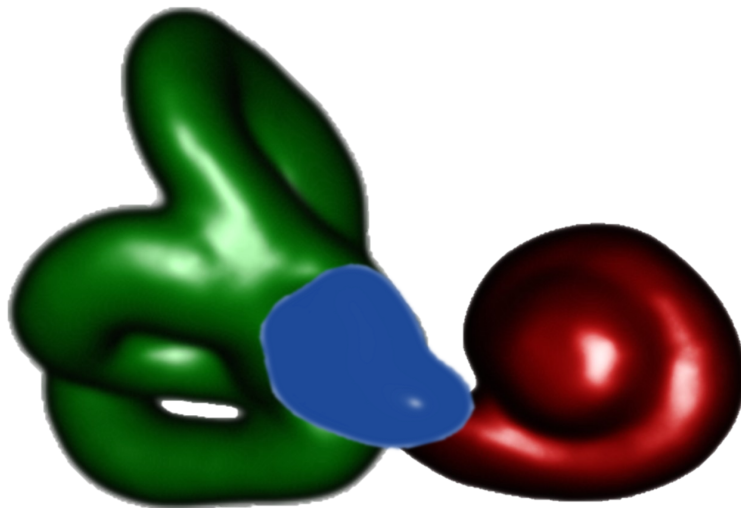
Figure 3.2: *Three dimensional visualization of the human inner ear probabilistic atlas for the bony labyrinth and extracted structures. The atlas components are distinguishable (cochlea in red; otolith organs in blue; semicircular canals in green) [1]*
.

Figure 3.3: *Three-dimensional visualization of produced atlas for right (right side) and left (left side) ear for cochlea and vestibule obtained by ImageVis3D-3.1.0. [141]*
.
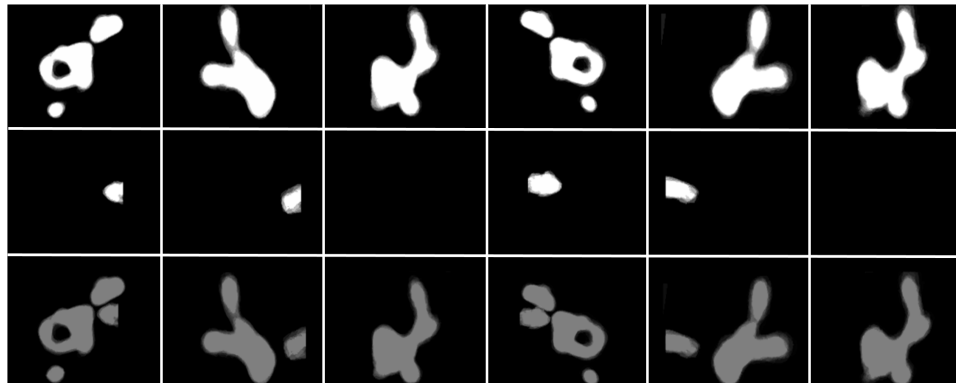
Figure 3.4: *Two-dimensional visualization of produced atlas for right (right side) and left (left ear) ear for cochlea and vestibule (first raw) and internal auditory meatus (second raw) in 3-scene view axial, coronal and sagittal view slice [93,-100,-97]. Last row shows the overlapping slice for the first and second raw. This atlas was previously published in [1]*

.

3.3 Proof of Valid Back Transformation for Deformable Registration with Plastimatch

In order to trust the back-transformation parameter during the registration workflow, we successfully proposed a methodology based on the manual models which verifies that applying the inverse transformation parameters on the registered model must yield to the original model. In figure 4.4, the effect of the deformable transformation on the CISS sequence VOI is shown for one sample subject. The VOI is resized and resampled according to the template space.

The SAD score is the sum of absolute differences between each voxel value and EBG which is the expert's binary grade, i.e. either 0 or 1. The product of EBG and SAD as the validation score of the back-transformation or inverse transformation of the registered models is presented for all subjects in table 3.3. Inner ears achieving lower than 95% of this score were considered as outliers and were eliminated before any processing.

Figure 3.5: *The axial view for the one slice result of deformable registration of one sample subject CISS sequence VOI using bspline deformable registration (left side) [26] and three dimensional view of the corresponding deformation effect on the binary inner ear model (right side)*

3.4 Atlas Performance in Atlas-Based Segmentation using Dice Score and RMSE of Control Points

In order to assess the accuracy of our obtained segmentation results, the dice score measurements in table 3.4 and the landmark registration error, as quantified by RMSE (see table 3.5), was calculated between the placed markers on the original data and the obtained landmarks on the segmented volumes. The standard deviation of RMSE and the mean values of it are calculated and shown in table 3.5. According to the reported values of the RMSE, the similarity of the left versus right side ears represents up to one voxel inequality. Moreover, the resulted statistics of testing dataset proves a precise match (the average of 3 voxels for testing set I and 5 voxels for testing set II). We used the two different testing sets I and II to support the advantage of our produced atlas for unseen subjects detected with the same pathology as the training set, and subjects with endolymphatic hydrops diagnosed with different pathology.

3.5 Main Impact Factors of Atlas Performance

In this part, we analyzed how the variation of registration parameters influences the performance of the overall atlas registration and segmentation. Increasing the population of the atlas dataset as well

as increasing the number of control points from 5 to 10 and 15 had a proportional relationship to the mean Dice score up to 3%. This advancement was the result of a more accurate registration since the absolute difference between the template and target image was improved from 7% to 2% for the left side and from 5% to 2% for the right side. Alteration the Gaussian filtering kernel size which was applied on the manually segmented models had an extreme effect on the performance of the atlas. In order to outline this effect, 10% increment in the mean value of the Dice score in the atlas-based segmentation was caused by two voxel reduction of the Gaussian kernel. We varried the kernel size starting from 3 voxels to 10 voxels (see figure 3.6). We used these analyses to find and set optimum values for the aforementioned parameters in the atlas construction pipeline. The mean value of the Dice score was 89% for the right side and 86% for the left side using the following parameters: number of the subjects in dataset = 24; Gaussian smoothing kernel = 5voxels; number of the control points = 5.
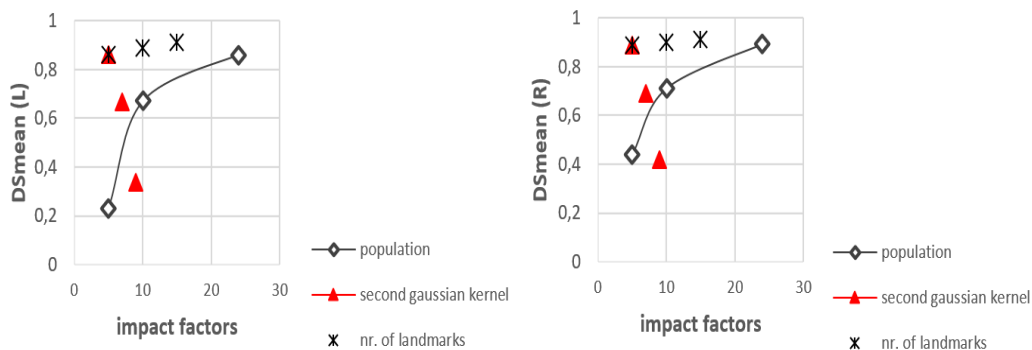
Figure 3.6: *Three major impact factors determining effectiveness on the mean Dice score measure for right and left sided inner ears using atlas-based segmentation with the training set. Population and number of landmarks have a proportional relationship with the performance measure while the second Gaussian kernel has an inverse relationship*

.

3.6 Inner Ear Lymphatic Fluid Extraction Validation

The segmentation results are presented in a qualitative matter in the visualization section and quantitative aspect in the performance analysis.

3.6.1   Segmentation Visualization

The atlas based segmentation of one sample subject is illustrated in figure 4.6 using three dimensional rendering software ImageVis3D `https://imagevis3d.software.informer.com/download/` and ITK Snap three-dimensional viewer toolbox `http://www.itksnap.org` [141] [139]. The ELS and PLS fluids are visualized in figure 4.8 and the original scans are shown after a histogram normalization was applied on those sequences.

Five patients with bilateral endolymphatic hydrops and five control subjects without endolymphatic hydrops (5 females; age range 20-70 years, mean age: 42.5 ± 6.2 years) underwent a high resolution MRI of the inner ears four hours after the intravenous administration of a Gadolinium-based contrast agent.. The step-wise segmentation consisted of three phases and was applied on the CISS and FLAIR images as shown in figure 4.8. After the three step multimodal segmentation was applied on CISS and FLAIR data, the binary results were thresholded to 0.5 for performance analysis. The dice score was applied on 3 different scenarios and for both right and left inner ears.
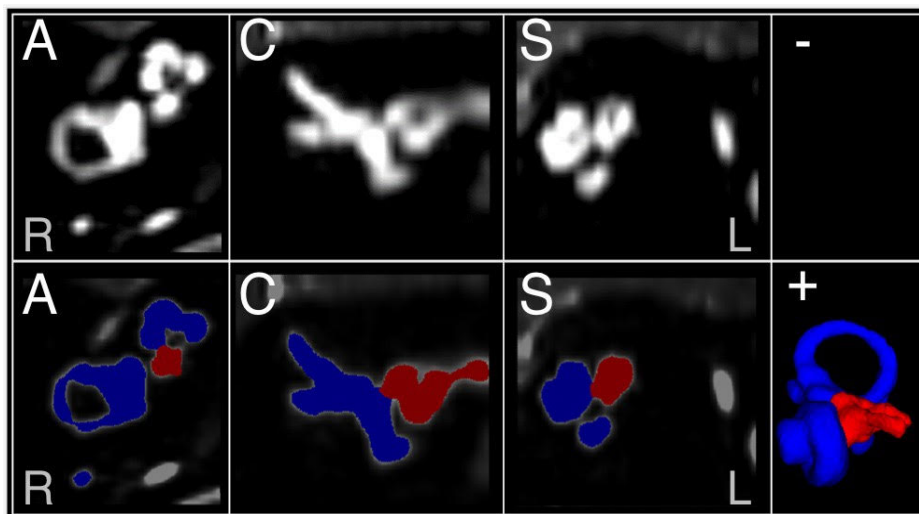
Figure 3.7: *One sample subject segmentation result visualization in the two and three dimensional space. The inner ear including cochlea, vestibule and circular canals (in blue color) is separated from the vestibulocochlear nerve and internal auditory meatus (in red color) using our two separated probabilistic atlases during the atlas-based segmentation [1].*

In figure 3.7, a segmentation process for one sample subject was

performed on a FLAIR sequence using random forest, and levelsets with active contours before the atlas-based segmentation; the extraction of the inner ear contrast enhanced ROI in the FLAIR sequence was successfully achieved.
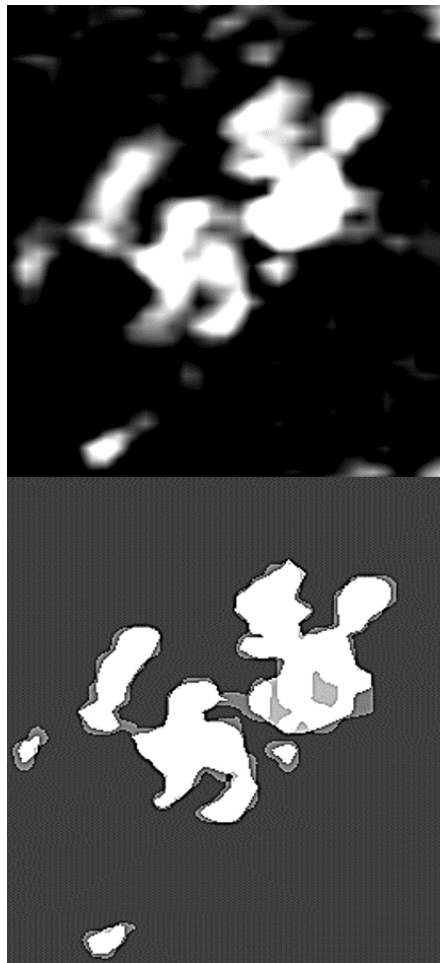
Figure 3.8: *Segmentation result of one sample subject; visualization on one axial slice in the two dimensional space. The extraction of the total inner ear lymphatic space and internal auditory meatus was performed before the atlas-based segmentation in order to verify the application of random forest method using levelsets with active contours in ITKsnap [139].*

3.6.2 Performance Analysis

The segmentation results are presented in a qualitative matter in the visualization section, while the quantitative aspects are provided in the performance analysis section. The analysis is divided into three different tables according to the reference standard applied and each segmentation was evaluated accordingly. Performance analysis for the

Figure 3.9: *Two and three dimensional visualization of the endolymph (EL) and perilymph (PL) segmentation [56]*

Figure 3.10: *Comparison between endolymph (EL) in yellow color, perilymph (PL) in blue color and total lymphatic space (TL) in white color segmentation in a healthy control subject right versus left side [56]*
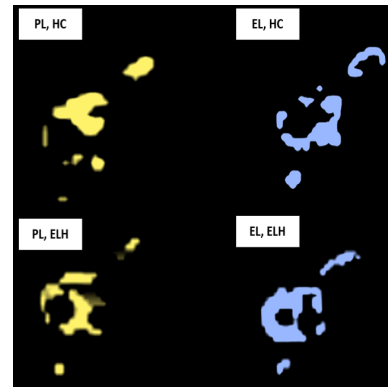
Figure 3.11: *Comparison between endolymph (EL) fluid in blue color and perilymph (PL) fluid in yellow color segmentation of the same slice in a normal inner ear (HC) versus in an inner ear with endolymphatic hydrops (ELH) [56]*

sequential multimodal segmentation approach for TLS, PLS and ELS in the human inner ear are summarized in tables 3.6, 3.7 and 3.8. Tables 3.6 to 3.8 present the validation scores and statistical parameters based on the segmentation obtained in this study. The values aligns to the atlas-based segmentation results from [1] in our previous study. Furthermore, the dice score values show a high overlap between the thresholding-based segmentation performed by experts, compared to the multimodal image segmentation in this study. Ultimately, the endolymphatic space was successfully extracted according

to the accuracy measures in table 3.8 for our datasets. Control subjects without endolymphatic hydrops showed 9% higher agreement for the ELS segmentation compared to the patients with endolymphatic hydrops. The dice score for segmentation of the PLS was 20% lower than the dice score for the ELS segmentation (compare Table 3.7).

Subject	EBG	SAD (R)	SAD(L)
1	1	0.014	0.031
2	1	0.011	0.022
3	1	0.22	0.13
4	1	0.0073	0.18
5	1	0.17	0.01
6	1	0.06	0.06
7	1	0.005	0.17
8	1	0.008	0.007
9	1	0.008	0.2
10	1	0.007	0.003
11	1	0.27	0.007
12	1	0.01	0.2
13	1	0.01	0.006
14	1	0.009	0.022
15	1	0.0034	0.0042
16	1	0.02	0.006
17	1	0.03	0.03
18	1	0.003	0.0008
19	1	0.1	0.098
20	1	0.01	0.01
21	1	0.001	0.003
22	1	0.006	0.11
23	1	0.02	0.2
24	1	0.056	0.039

Table 3.3: Validation of the fusion process using sum of absolute difference (SAD) score and experts binary grade (EBG) for both right and left ears using the atlas production dataset or training set with 24 subjects.

Property	Dice Score(Right)	Dice Score(Left)
Max	92%	90%
Min	64%	67%
Std.Dev.	±3%	±5.7%
Mean	89%	86%

Table 3.4: Dice score measure for automatic atlas-based segmentation results considering manual segmentation as a ground truth and the total volume of peripheral vestibular systems organs (PVSO) vestibule, cochlea and semi-circular canals. The standard deviation and mean values of the whole population for both sides are also presented [1].

Datasets:	SOURCE SET	TESTING SET I	TESTING SET II
Sides:	Right – Left	Right – Left	Right – Left
Mean of error:	5.79 – 6.93	17.55 – 18.06	19.59 – 21.55
RMSE:	2.56 – 2.63	4.19 – 4.25	4.42 – 4.64
$\frac{RMSE}{Emax-Emin}$:	0.024 – 0.026	0.061 – 0.064	0.083 – 0.085
Std. Error of Mean:	1.83 – 1.78	2.43 – 2.38	2.557 – 2.274

Table 3.5: Accuracy evaluation using the error of landmark positions between atlas-based segmentation and manual segmentation. Source dataset is the training dataset or included subjects' data to build the atlas 2.1[1].

Property	Healthy control subjects (HCS)	Patients with endolymphatic hydrops (PELH)
	Right – Left	Right – Left
$Mean_{DS}$ ±$Std_{dev.}$	89.9 ±0.3 − −85.1 ± 0.7	86 ±1.3 − −84 ± 2.4
Min_{DS}	66 – 60	67 – 63
Max_{DS}	91 – 90	90 – 86

Table 3.6: Quantitative scores for the step 1 of sequential multi-modal segmentation pipeline using atlas [1]-based segmentation and the manual gold standard ground truth from expert (GS1). As expected from the dice overlap score values, according to the validation process in [1], it shows an agreement between both sides as well as the reported values in [1].

Property	Healthy control subjects (HCS)	Patients with endolymphatic hydrops (PELH)
	Right – Left	Right – Left
$Mean_{DS}$ $\pm Std_{dev.}$	$91.8 \pm 0.1 - -92 \pm 0.3$	$86 \pm 0.3 - -84 \pm 1$
Min_{DS}	$88 - 88$	$67 - 63$
Max_{DS}	$94 - 93$	$89 - 87$

Table 3.7: Quantitative scores for the step 2 of sequential multi-modal segmentation pipeline using the supervised learning with level-sets and active contours using the FLAIR sequence and the extracted bony structure from the step 1 in CISS sequence as a multimodal image segmentation problem. The resulted segmentation shows the perilymphatic space. The ground truth is defined as GS2, which is the linear subtraction of GS1 and GS3 [13]

Property	Healthy control subjects (HCS)	Patients with endolymphatic hydrops (PELH)
	Right – Left	Right – Left
$Mean_{DS}$ $\pm Std_{dev.}$	$79 \pm 0.1 - -79 \pm 0.3$	$70 \pm 3.5 - -66 \pm 4.6$
Min_{DS}	$79 - 75$	$45 - 38$
Max_{DS}	$80 - 89$	$81 - 86$

Table 3.8: Quantitative scores for the step 3 of sequential mul-timodal segmentation pipeline using the subtraction techniques with nonlinear interpolation to obtain the PLS from the FLAIR sequence. The gold standard GS3 is defined as an interactive experts thresholding-based segmentation with a variant thresholding value depending on each individual subject data

Chapter 4

Discussion

In the studies underlying this dissertation, a probabilistic atlas for the labyrinth of the human inner ear was produces [1]. The atlas was generated using a set of volumetric data from CISS sequences collected from 24 subjects with vestibular migraine without endolymphatic hydrops. Several impact factors were detected during registration which influenced the accuracy of the registration, and therefore the performance of the final produced atlas [1] and in this study we attempted to investigate amongst the impact factors and optimized our atlas accordingly [1]. In our work, we found it necessary to note the importance of the control points placements and consider the optimal number of landmarks in distributed spots in the spatial space [1].

Recent projects proposed either manual or semi-automatic segmentation approaches for the inner ear in order to achieve a volume-based assessment [6],[10],[9]. Those mentioned methodologies, however, suffer from lengthy user interaction that hinder usage in larger group studies or in a clinical routine setting. In addition, they can concentrate on one single objective. Here, our proposed atlas-based segmentation could potentially be time-saving and less user-dependent. In addition, the atlas is applicable as a mask extractor for the inner ear on different co-registered sequences rather than the CISS sequence alone for further assessment.

Although many studies present an atlas production pipeline for different anatomies and organs of human or animals [32],[33],[34],[43],[45], choosing the best registration and probabilistic map construction method has always been a challenge. We aimed to solve the problem of inner ear segmentation by generating a probabilistic atlas [32] and

proposing an objective and reproducible segmentation method based on deformable registration provided by the 3D-slicer software [25],[26]. There was a strong harmony between the segmentation used by our atlas, and the standard models during the performance evaluation stage [1].

4.1   Challenges and Limitations

We reported a proportional correlation between the amount of landmarks and the mean value of the Dice score. This correlation was held regarding to the amount of dataset used to produce the atlas. Our experiments indicate that including more subjects as a source during template building in-creased the realism and utility of the resulting template and atlas: including the total number of subjects in the dataset which is 24 instead of a randomly selected set of 5 subjects, impacted the mean Dice score up to 50% for the right side and 60% for the left side. Three different Gaussian smoothing kernels [38] were applied to the label models, and with an optimum value of the kernel set to 5 voxels, the evaluation showed an improvement of segmentation up to 50%. We established a successful integration of the atlas information into the standard segmentation and the mean Dice score of 89% for the right side and 86% for the left side.

There are several limitations that need to be considered when interpreting the results of these studies. First, the sample size is limited in the various groups, especially for the segmentations of the endolymphatic and peripylmphatic spaces. Future studies with larger sample sizes with varying degrees of endolymphatic hydrops are needed to further corroborate our results. In addition, further optimization techniques could be considered, including a deep learning algorithm instead of a random forest for training.

Our algorithm showed overestimation of the structure due to assigning probabilistic values near boundaries. This effect can be rectified by enhancing the registration accuracy using more control points. The atlas production was performed using subjects with vestibular migraine without signs of endolymphatic hydrops. The fact that the models for atlas generation are directly built manually in an advanced phase,

a higher performance score could potentially be obtained by a more accurate expert segmentation. An averaging of two or three different ground truth may help the final validation measurement scores.

4.2 Application and Conclusion

The main result of the studies underlying this dissertation, the probabilistic atlas, can be applied as a basis for the analysis of various modalities of inner ear data. The probabilistic label assignment has straightforward applications since it is of great interest to investigate endolymph and perilymph spaces in different disorders, including *Menière's* disease [5],[9],[10],[11]. Due to the similar intensity distribution of the vestibulocochlear nerves to the lymphatic spaces in the contrast enhanced images of the inner ear, presenting location as a feature, which is achieved by our atlas, simplifies the lymphatic spaces segmentation in future experiments. The produced atlases for the left and right inner ears resulted in a 4.7% discrepancy. Individual inner ears demonstrate a $3-8\%$ difference between two sides which is congruent with our atlas. A multimodal stepwise segmentation algorithm for the endolymphatic and perilymphatic spaces was achieved furthering our previous publication in [2] [1]. This method will be a vital step toward the creation of an atlas of the endolymphatic and perilymphatic spaces. The segmentation method was validated in each step according to the corresponding reference standard.

In this study, to the best of our knowledge, we present the first MRI-derived 3D atlas of the labyrinth in the human inner ear, along with a semi-automatic atlas-based segmentation approach that was validated on prospective subjects with different pathologies. Our atlas provides in-vivo, computer-aided volumetric quantification of total lymphatic space. This study which proposed a novel methodology is considered to be an appropriate solution to detect ELH in curative and medical trials in *Menière's* disease.

In future studies, the atlas-based generated mask should be applied to T2-weighted FLAIR images [52],[13],[14]. The volumetric assessment of the fluid components inside the inner ear labyrinth will present a measurement tool to grade the endolymphatic hydrops.

Appendix A

Publication

- A probabilistic atlas of the human inner ear's bony labyrinth enables reliable atlas-based segmentation of the total fluid space, Valerie Kirsch, Fatemeh Nejatbakhshesfahani, S-Ahmad Ahmadi, Marianne Dieterich, Birgit Ertl-Wagner, Journal of Neurology pp 1-10, `https://doi.org/10.1007/s00415-019-09488-6`, August 2019

- P122. Multimodal probabilistic atlas of the human inner ear enables an automated and reliable segmentation of the endolymphatic space, F Nejatbakhshesfahani, V Kirsch, A Berman, D Keeser, A Ahmadi, M Dieterich, B Ertl-Wagner, Elsevier, Clinical Neurophysiology 129 (8), e112-e113, `https://doi.org/10.1016/j.clinph.2018.04.736`, August 2018

- Multimodal probabilistic atlas of the human inner ear enables an automated and reliable segmentation of the endolymphatic space, F Nejatbakhshesfahani, V Kirsch, A Berman, D Keeser, A Ahmadi, M Dieterich, B Ertl-Wagner, P122, DGKN 2018

- Poster: Towards an atlas of the endolymphatic space, F Nejatbakhshesfahani, A Ahmadi, M Dieterich, B Ertl-Wagner, V Kirsch, DIZZYNET 2018

Appendix B

Abbreviations

CISS	constructive interference in steady-state
ELH	endolymphatic hydrops
ELS	endolymphatic space
FLAIR	fluid attenuated inversion recovery
MRI	magnetic resonance imaging
L	left
LH	left-handed
MRI	magnetic resonance imaging
MD	Menière's disease
MRI	magnetic resonance imaging
R	right
RH	right-handed
TNOV	total number of voxels
TV	total volume
VM	vestibular migraine
IR	inversion recovery
GBCA	Gadolinium based contrast agent

SD   standard deviation

DS   Dice score

MIP   maximum intensity projection

Bibliography

[1] Kirsch, V., Nejatbakhshesfahani, F., Ahmadi, SA. et al., : A probabilistic atlas of the human inner ear's bony labyrinth enables reliable atlas-based segmentation of the total fluid space J Neurol (2019). https://doi.org/10.1007/s00415-019-09488-6

[2] Nejatbakhshesfahani, F., Kirsch, V., Berman, A., Keeser, D., Ahmadi, A., Dieterich, M., Ertl-Wagner, B.: P122. Multimodal probabilistic atlas of the human inner ear enables an automated and reliable segmentation of the endolymphatic space Clinical Neurophysiology **129 (8)**, e112–e113 (2018)

[3] Havia, M., Kentala, E., Pyykko, I.: Prevalence of Meniere's disease in general population of Southern Finland. Head Neck Surg. **133(5)**, 762–768 (2005)

[4] Alec, N. Salt, Stefan, K. Plontke, Bork, P.: Endolymphatic hydrops: pathophysiology and experimental models. Otolaryngol Clin North Am. **43(5)**, 971–983 (2010)

[5] Bara'th, K., Schuknecht, B., Monge Naldi, A., Schrepfer, T., Bockisch, C.J., Hegema, S.C.A.: Detection and grading of Endolymphatic Hydrops in Meniere Disease using MR imaging. American Journal of Neuroradiology **35(7)**, (2014)

[6] Timothy, C. Hain, MD, MRI imaging of Meniere's disease/syndrome Chicago Dizziness and Hearing.

[7] Shinji Naganawa, MD., Shunichi Ishihara, MD., Shingo Iwano, MD., Michihiko Sone, MD., Tsutomu Nakashima, MD.: Three-Dimensional (3D) Visualization of Endolymphatic Hydrops after Intratympanic Injection of Gd-DTPA: Optimization of a 3D-Real

Inversion-Recovery Turbo Spin-Echo (TSE) Sequence and Application of a 32-Channel Head Coil at 3T. Journal of Magnetic Resonance Imaging **10, Issue 2, pages 101-106**, (2011)

[8] Ilmari Pyykko, MD., Jing Zou, MD., Dennis Poe, MD., Tsutomu Nakashima, MD., Shinji Naganawa, MD.: Magnetic Resonance Imaging of the Inner Ear in Meniere's Disease. olaryngol Clin N Am. Elsevier Inc. **43**, (2010)

[9] Georg Homann, , Volker Vieth, , Daniel Weiss, , Konstantin Nikolaou, , Walter Heindel, . Mike Notohamiprodjo, , Yvonne Böckenfeld, : Semi-Quantitative vs. Volumetric Determination of Endolymphatic Space in Menière's Disease Using Endolymphatic Hydrops 3T-HR-MRI after Intravenous Gadolinium Injection. journal.pone.0120357 **DOI:10.1371**, (2015)

[10] Gürkov, R., Berman, A., Dieterich, O., Flatz, W., Jerin, C.. Krause, E., Keeser, D., Ertl-Wagner, B.: MR volumetric assessment of endolymphatic hydrops. Eur Radiol. **DOI 10.1007/s00330-014-3414-4 HEAD AND NECK**, (2015)

[11] Horii, A., Osaki, Y., Kitahara, T., Imai, T., Uno, A.. Nishiike, S., Fujita, N., Inohara, H.: Endolymphatic hydrops in Meniere's disease detected by MRI after intratympanic administration of gadolinium: Comparison with sudden deafness. Journal Acta Oto-Laryngologica, PubMed Acta Oto-Laryngologica, 2011 **131**, 602–609 (2011)

[12] Homann, G., Böckenfeld, Y., Basel, T., Heindel, W., Vieth, V.. Nishiike, S., Fujita, N., Inohara, H.: Quantitative evaluation of endolymphatic hydrops and acceptance testing in patients with Menière's disease. European society of radiology **10.1594**, (2014)

[13] Sepahdari, A.R., Ishiyama, G., Vorasubin, N., Peng, K.A., Linetsky, M.. Ishiyama, A.: Delayed intravenous contrast-enhanced 3D FLAIR MRI in Meniere's disease: correlation of quantitative measures of endolymphatic hydrops with hearing. Clin Imaging **39(1)**, 26–31 (2015)

[14] Sepahdari, A.R., Vorasubin, N., Ishiyama, G., Ishiyama, A.: Endolymphatic Hydrops Reversal following Acetazolamide Therapy: Demonstration with Delayed Intravenous Contrast-Enhanced 3D-FLAIR MRI. AJNR Am J Neuroradiol **37(1)**, 151–154 (2016)

[15] Nakashima, T., Naganawa, S., Pyykko, I., Gibson, W.P., Sone, M., Nakata, S., Teranishi, M.: Grading of endolymphatic hydrops using magnetic resonance imaging. Acta Otolaryngol Suppl **129**, 5–8 (2009)

[16] Sharma, N., M. Aggarwal, L.: Automated medical image segmentation techniques. J Med Phys **35(1)**, 3–14 (2010)

[17] Cabezas, M., Oliver, A., Lladó, X., Freixenet, J.. Cuadra, M.B.: A review of atlas-based segmentation for magnetic resonance brain images. Comput Methods Programs Biomed **104(3)**, 158–177 (2011)

[18] Christensen, G.E., He, J., Dill, J.A., Rubinstein, J.T., Vannier, M.W.. Wang, G.: Automatic measurement of the labyrinth using image registration and a deformable inner ear atlas. Academic Radiology, Published by Elsevier **10, Issue 9**, 988–999 (2003)

[19] Meng, J., Zhang, F., Li, Q., Qin, Z.: Cochlear Size and Shape Variability and Implications in Cochlear Implantation Surgery. Otol Neurotol **37(9)**, 1307–1313 (2016)

[20] Toga, A.W., Thompson, P.M.: The role of image registration in brain mapping. Image Vis Comput **19(1-2)**, 3–24 (2009)

[21] Scheel, V., Hofmann, M., Rehfeld, N., Judenhofer, M.S.: Claussen, C.D.. Pichler, B.J.: Evaluation of Deformable Registration Methods for MR-CT Atlas Alignment. IEEE Nuclear Science Symposium and Medical Imaging Conference (NSS-MIC 2007) **2007, Issue M13-121**, 1– (2007)

[22] Rueckert, D., Sonoda, L. I., Hayes, C., Hill, D. L. G.: Leach, M. O.. Hawkes, D. J.: Nonrigid Registration Using Free-Form Deformations: Application to Breast MR Images. EEE TRANSACTIONS ON MEDICAL IMAGING **18**, (1999)

[23] Vincent, Charvillat, Adrien, Bartoli, Hayes, C., Hill, D. L. G.: Leach, M. O.. Hawkes, D. J.: Feature-based estimation of radial basis mappings for non-rigid registration. VMV 2005 Erlangen Germany (2005)

[24] Sharp, G.C., Li, R., Wolfgang, J., Chen, C., Peroni, M.. Spadea, M. F., Mori, S., Zhang, J., Shackleford, J., Kandasamy, N.: Plastimatch-An open source softwaresuite for radiotherapy image processing. Proceedings of the XVI'th International Conference on the use of Computers in Radiotherapy (ICCR),Amsterdam,Netherlands (2009)

[25] Wu, Z., Rietzel, R.E., Boldea, V., Sarrut, D., Sharp, G.C: Evaluation of deformable registration of patient lung 4DCT with subanatomical region segmentations. MedicalPhysics **35(2)**, 775–781 (2008)

[26] Sharp, G.C: Deformable Image Registration Using B-Splines. Massachusetts General Hospital, Radiation Oncology (2011)

[27] Penney, G.P., Weese, J., Little, J.A., Desmedt, P., Hawkes, D.J.: A comparison of similarity measures for use in 2-D-3-D medical image registration. IEEE Trans Med Imaging **17(4)**, 586–595 (1998)

[28] Craene, M. De, Aische, A. B. d, Macq, B., Warfield, S.K.: Multi-subject registration for unbiased statistical atlas construction. Proceedings of MICCAI, Springer-Verlag Berlin Heidelberg **LNCS 3216**, 655–662 (2004)

[29] Akinola Olanrewaju Akinyemi, Meng: Atlas-Based Segmentation of Medical Images. EngD thesis, Glasgow university (2011)

[30] Bilello, M., Lao, Z., Krejza, J., Hillis, AE., Herskovits, EH.: Atlas-Based Classification of Hyperintense Regions from MR Diffusion-Weighted Images of the Brain. Neuroradiol J. Epub **25(1)**, 112–120 (2012)

[31] Carmichael OT, Aizenstein HA, Davis SW et al, : Atlas-Based Hippocampus Segmentation In Alzheimer's Disease and Mild Cognitive Impairment. Neuroimage **27(4))**, 979–990 (2005)

[32] Kaikai, Shena, Pierrick, Bourgeat, Jurgen, Fripp, Fabrice, Meriaudeau, David, Ames, Kathryn, A. Ellise, Colin, L. Masterse, Victor, L. Villemagned, Christopher, C. Rowe, Olivier, Salvado: Supervised Method to Build an Atlas Database for Multi-atlas Segmentation-propagation. Medical Imaging 2010: Computer-Aided Diagnosis, edited by Nico Karssemeijer, Ronald M. Summers, Proc. of SPIE **7624**, (2010)

[33] Russell, Taylor, Xin, Kang(Ben), Ceylan, Tanes, Murat, Bilgel: Statistical Atlas of the Knee. Computer Integrated Surgery, Johns Hopkins University **600.446**, (2011)

[34] Chintalapani, G.: Statistical Atlases of Bone Anatomy and Their Applications. Engineering Research Center for Computer Integrated Surgical Systems and Technology Johns Hopkins University (2010)

[35] Zöllei, L., Shenton, M., Wells III, W.M., Pohl, K.M.: The Impact of Atlas Formation Methods on Atlas-Guided Brain Segmentation, Statistical Registration. Tenth International Conference on Medical Image Computing and Computer-Assisted Intervention, Brisbane, Australia 39–46 (2007)

[36] Chakravarty, M.M., Bertrand, G., Hodge, C.P., Sadikot, A.F., Collins, D.L.: The creation of a brain atlas for image guided neurosurgery using serial histological data. Neuroimage, Epub **30(2)**, 259–376 (2006)

[37] Walker, M.: Vestibular System. Encyclopedia of the Neurological Sciences (Second Edition) (2014)

[38] Verma, A., Asst. Prof. Mishra, A., Hodge, C.P., Sadikot, A.F., Collins, D.L.: Image Compression using Gaussian Smoothing Filter and Median Filter. International Journal on Recent and Innovation Trends in Computing and Communication **ISSN: 2321-8169Volume: 3Issue: 116344-6347**, (2015)

[39] Ferreira, A., Gentil, F., Manuel R. S. Tavares, J.: Segmentation Algorithms for Ear Image Data towards Biomechanical Studies. CMBBE **17(8)**, 888–904 (2014)

[40] Commowick, O., Malandain, G.: Evaluation of Atlas Construction Strategies in the Context of Radiotherapy Planning. MICCAI (2006)

[41] Stuart, M. Grieve, Obholzer, R., Malitz, N., P. Gibson, W., D. Parker, G.: Imaging of endolymphatic hydrops in Meniere's disease at 1.5 T using phase-sensitive inversion recovery: (1) Demonstration of feasibility and (2) overcoming the limitations of variable gadolinium absorption. European Journal of Radiology **81**, 331–338 (2012)

[42] Hyunjin, Park: Adaptive Registration and Atlas Based Segmentation. Doctor of Philosophy dissertation (Biomedical Engineering) in The University of Michigan (2003)

[43] Otaky, N., Paus, T., D'Avirro, D., Gutmans, D., MacDonald, D., Caramanos, Z., Tomaioulo, F, Evans, AC.: Volumetric Analysis of the Human Cingulate, Paracingulate, and Superior Rostral Sulci. Society for Neuroscience Abstracts **21**, 1–154 (1995)

[44] Thompson, PM., MacDonald, D., Mega, MS., Holmes, CJ., Evans, AC., Toga, AW.: Detection and Mapping of Abnormal Brain Structure with a Probabilistic Atlas of Cortical Surfaces. J. Comp. Assist. Tomogr. **21(4)**, 567–581 (1997)

[45] Paus, T., Tomaioulo, F., Otaky, N., MacDonald, D., Petrides, M., Atlas, J., Morris, R., Evans, AC.: Human Cingulate and Paracingulate Sulci. Pattern, Variability, Asymmetry and Probabilistic Map, Cerebral Cortex **6**, 207–214 (1996)

[46] Evans, AC., Collins, DL., Milner, B.: An MRI-based Stereotactic Brain Atlas from 300 Young Normal Subjects. Proceedings of the 22nd Symposium of the Society for Neuroscience, Anaheim **408**, (1992)

[47] Evans, AC., Collins, DL., Neelin, P., MacDonald, D., Kamber, M., Marrett, TS.: Three-Dimensional Correlative Imaging: Applications in Human Brain Mapping. Functional Neuroimaging 145–162 (1994)

[48] Enache, T., Enache, A.: Our Experience with the Medical Treatment of Endolymphatic Hydrops. International Tinnitus Journal **13(2)**, 138–142 (2007)

[49] Brown, Daniel, Enache, A.: Potential Causes of Endolymphatic Hydrops and Ménière's Disease. The University of Sydney (2014)

[50] Richardson, M.: Hearing and balance. Part 4–Nervous pathways and related problems. Nurs Times (2007)

[51] Gürkov, R., Pyyko, I., Zou, J., Kentala, E.: A contemporary re-evaluation of endolymphatic hydrops. J Neurol. **263 (Suppl 1)**, 71–81 (2016)

[52] Hagiwara M, , Roland JT Jr, , Wu X, , Nusbaum A, , Babb JS, , Roehm PC, , Hammerschlag P, , Lalwani AK, , Fatterpekar G, : Identification of endolymphatic hydrops in Ménière's disease utilizing delayed postcontrast 3D FLAIR and fused 3D FLAIR and CISS color maps. Otol Neurotol. **35(10)**, 337–342 (2014)

[53] Varsha M. Joshi, , Shantanu K. Navlekar, , G. Ravi Kishore, , K. Jitender Reddy, , E. C. Vinay Kumar, : CT and MR Imaging of the Inner Ear and Brain in Children with Congenital Sensorineural Hearing Loss. Neurologic/Head and Neck Imaging **32 Issue 3**, (2012)

[54] Zou, KH, Warfield, SK, Baharatha, A, Tempany, C, Kaus, MR, Haker, SJ, , et al.: Statistical validation of image segmentation quality based on a spatial overlap index. Academic Radiology **11**, 178–189 (2004)

[55] Stephen, Yip, Timothy, Perk, Robert, Jeraj: Development and evaluation of an articulated registration algorithm for human skeleton registration. Physics in Medicine and Biology **59(6)**, 1485 (2014)

[56] Liu, IY, Sepahdari, AR, Ishiyama, G, Ishiyama, A: High Resolution MRI Shows Presence of Endolymphatic Hydrops in Patients Still Symptomatic After Endolymphatic Shunt Surgery. Otol Neurotol **37(8)**, 1128–1130 (2016)

[57] Brandt, T., Dieterich, M.: The dizzy patient: don't forget disorders of the central vestibular system Nat Rev Neurol. **13(6)**, 352–362 (2017)

[58] Nakada, T., Yoshida, T., Suga, K., Kato, M., Otake, H., Kato, K., Teranishi, M., Sone, M., Sugiura, S., Kuno, K., Pyykkö, I., Naganawa, S., Watanabe, H., Sobue, G., Nakashima, T.: Endolymphatic space size in patients with vestibular migraine and Ménière's disease Journal of Neurology **261 (11)**, 2079–2084 (2014)

[59] Purves, Dale, Augustine, George J, David, Fitzpatrick, Lawrence C, Katz, Anthony-Samuel, LaMantia, James O, McNamara, S Mark, Williams: Neuroscience, 2nd edition Sunderland (MA): Sinauer Associates **Chapter 14**, (2001)

[60] Khan, S., Chang, R: Anatomy of the vestibular system: a review Sunderland (MA): Sinauer Associates **32(3)**, 437–443 (2013)

[61] Mangabeira, Pedro Luiz Albernaz, Zuma e Maia, Francisco, Carmona, Sergio, Rodrigues Cal, Renato Valério, Anthony-Samuel, LaMantia, Zalazar, Guillermo: The Vestibular Syndromes The New Neurotology 115–132 (2019)

[62] Magnan, Jacques, Özgirgin, O. Nuri, Trabalzini, Franco, Lacour, Michel, Lopez Escamez, Antonio, Magnusson, Mans, Alpin Güneri, Enis, Guyot, Jean Philippe , Nuti, Daniele, Mandalà, Marco: European Position Statement on Diagnosis, and Treatment of Meniere's Disease J Int Adv Otol **14(2)**, 317–321 (2018)

[63] Rebillard, G., Pujol, R: cochlea: overview Producer: Association NeurOreille (2016)

[64] Teixido, M.: Meniere Disease `http://entad.org/for-patients/patient-information-dr-teixido/endolymphatic-hydrops-menieres-disease/`

[65] Information about Hearing, Communication, and Understanding NIH Curriculum Supplement Series [Internet].National Institutes of Health (US); Biological Sciences Curriculum Study. Bethesda (MD): National Institutes of Health (US) (2007)

[66] `https://www.mybiosource.com/learn/endolymphatic-hydrops/` Designed by Elegant Themes — Powered by WordPress (2007)

[67] Tsutomu Nakashima, MD., Shinji Naganawa, MD.: Visualization of endolymphatic hydrops with MR imaging in patients with Ménière's disease and related pathologies: current status of its methods and clinical significance. Japanese Journal of Radiology **32(4)**, 191–204 (2014)

[68] Mandy Mroz, AuD.: Meniere's disease `https://www.healthyhearing.com/help/tinnitus/menieres-disease` (2019)

[69] Fraysse BG, , Alonso A, , House WF, : Ménière's disease and endolymphatic hydrops: clinical-histopathological correlations Ann Otol Rhinol Laryngol Suppl **89**, 2–22 (1980)

[70] Pyykko I, , Arroll MA, , Nakashima T, MD.: Meniere's disease. Nat Rev Dis Prim **2 doi: 10.1038/nrdp.2016.28**, 16028 (2016)

[71] Rauch SD, , Merchant SN, , Thedinger BA , : Meniere's syndrome and endolymphatic hydrops. Double-blind temporal bone study. Ann Otol Rhinol Laryngol **98**, 873–883 (1989)

[72] Sepahdari, A.R., Ishiyama, G., Lopez, IA., Ishiyama, A.: Meniere's disease: histopathology, cytochemistry, and imaging.. Ann N Y Acad Sci **1343**, 49–57 (2015)

[73] Gürkov, R., Pyyko, I., Zou, J. et al.: Imaging of Temporal Bone. Advances in oto-rhino-laryngology 12–13 (2019)

[74] Lopez-Escamez JA, , Attyé A, : Magnetic resonance imaging of endolymphatic hydrops: Controversies and common ground. J Vestib Res 1–4 (2019)

[75] Naganawa S, , Satake H, , Kawamura M, et al, : Separate visualization of endolymphatic space, perilymphatic space and bone by a single pulse sequence; 3D-inversion recovery imaging utilizing real reconstruction after intratympanic Gd-DTPA administration at 3 Tesla. Eur Radiol **18**, 920–924 (2008)

[76] Naganawa S, , Yamazaki M, , Kawai H, et al, : Visualization of endolymphatic hydrops in Ménière's disease with single-dose intravenous gadolinium-based contrast media using heavily T(2)-weighted 3D-FLAIR. Magn Reson Med Sci **9**, 237–242 (2010)

[77] Attyé A, , Eliezer M, , Galloux A, et al, : Endolymphatic hydrops imaging: Differential diagnosis in patients with Meniere disease symptoms. Diagn Interv Imaging **98**, 699–706 (2017)

[78] Imai T, Uno A, Kitahara T, et al, : Evaluation of endolymphatic hydrops using 3-T MRI after intravenous gadolinium injection. Eur Arch Oto-Rhino-Laryngology **274**, 4103–4111 (2017)

[79] Karch-Georges A, Veillon F, Vuong H, et al, : MRI of endolymphatic hydrops in patients with vestibular schwannomas: a case-controlled study using non-enhanced T2-weighted images at 3 Teslas.. Eur Arch Oto-Rhino-Laryngology **276**, 1591–1599 (2019)

[80] Kirsch V, Ertl-Wagner B, Berman A, et al, : MRI of the inner ear enables differentiation of central and peripheral vestibular pathologies in a postoperative ELST patient - A single case study. J Neurol in print (2018)

[81] Sun W, Liang Q, Kuang S, et al, : 3D-real IR MRI detects serendipity of inner ear in enlarged vestibular aqueduct syndrome. Acta Otolaryngol **139**, 233–237 (2019)

[82] Conte G, Caschera L, Tuscano B, et al, : Three-Tesla magnetic resonance imaging of the vestibular endolymphatic space: A systematic qualitative description in healthy ears. Eur J Radiol **109**, 77–82 (2018)

[83] Lobo D, Tuñón M, Villarreal I, et al, : Intratympanic gadolinium magnetic resonance imaging supports the role of endolymphatic hydrops in the pathogenesis of immune-mediated inner-ear disease. J Laryngol Otol **132**, 554–559 (2018)

[84] Neff B a., Staab JP, Eggers SD, et al, : Auditory and Vestibular Symptoms and Chronic Subjective Dizziness in Patients With Ménière's Disease, Vestibular Migraine, and Ménière's Disease

With Concomitant Vestibular Migraine. Otol Neurotol **33**, 1235–1244 (2012)

[85] Naganawa S, Suzuki K, Nakamichi R et al, : Semi-quantification of endolymphatic size on MR imaging after intravenous injection of single-dose gadodiamide: comparison between two types of processing strategies. Magn Reson Med Sci **12**, 261–269 (2013)

[86] Zwergal A, Kirsch V, Gerb J et al, : Neuro-otology: at the borders of ear and brain. Nervenarzt **89**, 1106–1114 (2018)

[87] Penney GP, Weese J, Little JA et al, : A comparison of similarity measures for use in 2-D-3-D medical image registration. IEEE Trans Med Imaging **17**, 586–595 (1998)

[88] Dieterich M, Bense S, Lutz S, et al, : Dominance for vestibular cortical function in the non-dominant hemisphere. Cereb Cortex **13**, 994–1007 (2003)

[89] Mansour SL, Schoenwolf GC, : Morphogenesis of the inner ear. In: Kelley M, Wu D, Popper A, Fay R (eds) Development of the inner ear. Springer, New York 43–84 (2005)

[90] Hatch EP, Noyes CA, Wang X et al, : Fgf3 is required for dorsal patterning and morphogenesis of the inner ear epithelium. Development **134**, 3615–3625 (2007)

[91] Dill T, : Contraindications to magnetic resonance imaging: non-invasive imaging. Heart **94**, 943–948 (2008)

[92] Lempert T, : Vestibular migraine. Semin Neurol **33**, 212–218 (2013)

[93] Lopez-Escamez JA, Carey J, Chung W-H et al, : Diagnostic criteria for Menière's disease. J Vestib Res **25**, 1–7 (2015)

[94] Dieterich M, Brandt T , : Ocular torsion and tilt of subjective visual vertical are sensitive brainstem signs. Ann Neurol **33**, 292–299 (1993)

[95] Schneider E, Villgrattner T, Vockeroth J, et al, : EyeSeeCam: an eye movement-driven head camera for the examination of natural visual exploration Ann N Y Acad Sci **1164**, 461–467 (2009)

[96] JONGKEES LB, MAAS JP, PHILIPSZOON AJ, : EClinical nystagmography. A detailed study of electro-nystagmography in 341 patients with vertigo Pract Otorhinolaryngol (Basel) **24**, 65–93 (1962)

[97] Oldfield RC, : The assessment and analysis of handedness: the Edinburgh inventory Neuropsychologia **9**, 97–113 (1971)

[98] Salmaso D, Longoni AM, : Problems in the Assessment of Hand Preference Cortex **21**, 533–549 (1985)

[99] Kirsch V, Ertl-Wagner B, Berman A et al, : High-resolution MRI of the inner ear enables syndrome differentiation and specific treatment of cerebellar downbeat nystagmus and secondary endolymphatic hydrops in a postoperative ELST patient J Neurol **265**, 48–50 (2018)

[100] Kirsch V, Becker-Bense S, Berman A, et al, : Transient endolymphatic hydrops after an attack of vestibular migraine: a longitudinal single case study J Neurol **265**, 51–53 (2018)

[101] Fedorov A, Beichel R, Kalpathy-Cramer J, et al, : Asymptotic stability of switching systems Magn Reson Imaging **30**, 1323–1341 (2012)

[102] Schindelin J, Arganda-Carreras I, Frise E, et al, : Fiji: an open-source platform for biological-image analysis Nat Methods **9**, 676–682 (2012)

[103] Liu F, Huang W, Meng X et al, : Comparison of noninvasive evaluation of endolymphatic hydrops in Meniere's disease and endolymphatic space in healthy volunteers using magnetic resonance imaging Acta Otolaryngol **132**, 234–240 (2012)

[104] Kendi TK, Arikan OK, Koc C, : Volume of components of labyrinth: magnetic resonance imaging study Otol Neurotol **26**, 778–781 (2005)

[105] Morita N, Kariya S, Deroee AF et al, : Membranous labyrinth volumes in normal ears and Ménière disease: a three-dimensional reconstruction study NIH public access Laryngoscope **119**, 2216–2220 (2009)

[106] Levy RB, Marquarding T, Reid AP et al, : Circuit asymmetries underlie functional lateralization in the mouse auditory cortex Nat Commun **10**, 1783 (2019)

[107] Tervaniemi M, Hugdahl K, : Lateralization of auditorycortex functions Brain Res Rev **43**, 231–246 (2003)

[108] Sininger YS, Bhatara A, : Laterality of basic auditory perception Laterality **17**, 129(2012)

[109] Janzen J, Schlindwein P, Bense S et al, : Neural correlates of hemispheric dominance and ipsilaterality within the vestibular system Neuroimage **42**, 1508–1518 (2008)

[110] Lopez C, Blanke O, Mast FW, : human vestibular cortex revealed by coordinate-based activation likelihood estimation meta-analysis. Neuroscience **221**, 159–179 (2012)

[111] Kirsch V, Boegle R, Keeser D et al, : Handedness-dependent functional organizational patterns within the bilateral vestibular cortical network revealed by fMRI connectivity based parcellation Neuroscience **178**, 224–237 (2018)

[112] Bense S, Bartenstein P, Lutz S et al, : Three determinants of vestibular hemispheric dominance during caloric stimulation: a positron emission tomography study Ann N Y Acad Sci **1004**, 440–445 (2003)

[113] Dieterich M, Kirsch V, Brandt T, : Right-sided dominance of the bilateral vestibular system in the upper brainstem and thalamus J Neurol `https://doi.org/10.1007/s00415-017-8453-8`,

[114] Mišić B, Betzel RF, Griffa A et al, : Network-based asymmetry of the human auditory system Cereb Cortex **28**, 2655–2664 (2018)

[115] Goni J, van den Heuvel MP, Avena-Koenigsberger A et al, : Resting-brain functional connectivity predicted by analytic measures of network communication Proc Natl Acad Sci **111**, 833–838 (2014)

[116] Andoh J, Matsushita R, Zatorre RJ, : Asymmetric interhemispheric transfer in the auditory network: evidence from TMS, resting-state fMRI, and diffusion imaging J Neurosci **35**, 14602–14611 (2015)

[117] Cammoun L, Thiran JP, Griffa A et al, : Intrahemispheric cortico-cortical connections of the human auditory cortex Brain Struct Funct **220**, 3537–3553 (2015)

[118] Boemio A, Fromm S, Braun A, Poeppel D, : Hierarchical and asymmetric temporal sensitivity in human auditory cortices Nat Neurosci **8**, 389–395 (2005)

[119] Dalca AV, Balakrishnan G, Guttag J, Sabuncu MR, : Hierarchical and asymmetric temporal sensitivity in human auditory cortices MICCAI: Medical image computing and computer assisted intervention `https://doi.org/10.1007/978-3-030-00928-1_82`, (2018)

[120] Dalca AV, Yu E, Golland P et al, : Unsupervised deep learning for Bayesian brain MRI segmentation MICCAI: Medical image computing and computer assisted intervention **arXiv :1904.11319**, (2019)

[121] Stojanov D, Aracki-Trenkic A, Benedeto-Stojanov D, : Gadolinium deposition within the dentate nucleus and globus pallidus after repeated administrations of gadolinium-based contrast agents—current status Neuroradiology **58**, 433–441 (2016)

[122] Moser FG, Watterson CT, Weiss S et al, : High signal intensity in the dentate nucleus and globus pallidus on unenhanced T1-weighted MR images: comparison between gadobutrol and linear gadolinium-based contrast agents Am J Neuroradiol **39**, 421–426 (2018)

[123] Boyken J, Frenzel T, Lohrke J et al, : Gadolinium accumulation in the deep cerebellar nuclei and globus pallidus after exposure to linear but not macrocyclic gadolinium-based contrast agents in a retrospective pig study with high similarity to clinical conditions Investig Radiol **53**, 278–285 (2018)

[124] Radtke A, von Brevern M, Neuhauser H et al, : Vestibular migraine: long-term follow-up of clinical symptoms and vestibulo-cochlear findings Neurology **79**, 1607–1614 (2012)

[125] Ito T, Kitahara T, Inui H et al, : Endolymphatic space size in patients with Meniere's disease and healthy controls Acta Otolaryngol **6489**, 1–4 (2016)

[126] Liu F, Huang W, Wang Z et al, : Noninvasive evaluation of endolymphatic space in healthy volunteers using magnetic resonance imaging Acta Otolaryngol **131**, 247–257 (2011)

[127] Lincoln Gray, Ph.D., : Chapter 10: Vestibular System: Structure and Function, Department of Communication Sciences and Disorders, James Madison University, `https://nba.uth.tmc.edu/neuroscience/m/s2/chapter10.html`, Department of Neurobiology and Anatomy - Site webmaster: `nba.webmaster@uth.tmc.edu`

[128] Jennifer Walinga, Royal Roads University, : Introduction to Psychology – 1st Canadian Edition, Publisher: BCcampus **Chapter 5.3 Hearing**, (2010)

[129] Guoqiang Wan, Gabriel Corfas, Jennifer S Stone, : Inner ear supporting cells: Rethinking the silent majority, Semin Cell Dev Biol **24(5)**, 448–459 (2013)

[130] Purves D, Augustine GJ, Fitzpatrick D, et al., : Neuroscience. 2nd edition, Sunderland (MA): Sinauer Associates (2001)

[131] Sebahattin Cureoglu, Rafael da Costa Monsanto, Michael M. Paparella, : Histopathology of Meniere's disease, Oper Tech Otolayngol Head Neck Surg. **27(4)**, 194–204 (2016)

[132] Shinji Naganawa, Masahiro Yamazaki, Hisashi Kawai, Kiminori Bokura, Michihiko Sone, Tsutomu Nakashima , : Imaging of Meniere's Disease by Subtraction of MR Cisternography from Positive Perilymph Image, Magn Reson Med Sci **11(4)**, 303–309 (2012)

[133] Govind B. Chavhan, Paul S. Babyn, Bhavin G. Jankharia, Hai-Ling M. Cheng, Manohar M. Shroff, : Steady-State MR Imaging Sequences: Physics, Classification, and Clinical Applications, RSNA, RadioGraphics **28(4)**, 1147–1160 (2008)

[134] Govind B. Chavhan, Paul S. Babyn, Bhavin G. Jankharia, Hai-Ling M. Cheng, Manohar M. Shroff, : Steady-State MR Imaging Sequences: Physics, Classification, and Clinical Applications, RSNA, RadioGraphics **28(4)**, 1147–1160 (2008)

[135] Sarbesh Tiwari, : MRI in inner ear pathology Congenital Inner ear anomalies `https://www.slideshare.net/sarbesh1984/magnetic-resonance-imaging-of-inner-ear`, Health and Medicine **28(4)**, 1147–1160 (2013)

[136] Shanshan Zhu, Wanrong Gao, Gang Yuan, et al. , : 3D automatic MRI level set segmentation of inner ear based on statistical shape models prior, IEEE, Image and Signal Processing, BioMedical Engineering and Informatics (CISP-BMEI), 10th International Congress **DOI:10.1109/CISP-BMEI.2017.8301973**, (2017)

[137] Miller, M.E. Bykowski, : Imaging Analysis of Ménière's Disease, J. Curr Otorhinolaryngol Rep **https://doi.org/10.1007/s40136-014-0056-7**, 2–152 (2014)

[138] Zou J, Pyykk¨ I, Yoshida T, Gürkov R, Shi H, Li Y, Zheng G, Zhao Z, Peng R, Zheng H, Yin S,Hyttinen J, Nakashima T and Naganawa S , : Milestone Research on Meniere's Disease by Visualizing Endolymphatic Hydrops Using Gadolinium-Enhanced Inner Ear MRI and the Challenges in Clinical Applications, Austin J Radiol. 2(6)–1035 (2015)

[139] Paul A, Yushkevich Yang Gao, Guido Gerig , : ITK-SNAP: an interactive tool for semi-automatic segmentation of multi-modality biomedical images., Conf Proc. IEEE Eng Med Biol Soc doi: 10.1109/EMBC.2016.7591443 (2016)

[140] Y. Duan, P.G. Hildenbrand, M.P. Sampat, D.F. Tate, I. Csapo, B. Moraal, R. Bakshi, F. Barkhof, D.S. Meier and

C.R.G. Guttmann, : Segmentation of Subtraction Images for the Measurement of Lesion Change in Multiple Sclerosis, American Journal of Neuroradiology **29(2)**, 340–346 (2008) https://doi.org/10.3174/ajnr.A0795

[141] CIBC, ImageVis3D, : ImageVis3D:An interactive visualization software system for large-scale volume data. Scientific Computing and Imaging Institute (2016) http://www.imagevis3d.org"

[142] Fedorov A., Beichel R., Kalpathy-Cramer J., Finet J., Fillion-Robin J-C., Pujol S., Bauer C., Jennings D., Fennessy F.M., Sonka M., Buatti J., Aylward S.R., Miller J.V., Pieper S., Kikinis R., : 3D Slicer as an Image Computing Platform for the Quantitative Imaging Network. Magn Reson Imaging. **30(9)**, 1323–1341 (2012) PMID: 22770690. PMCID: PMC3466397.

Acknowledgements

Success is best when it's shared- Howard Schultz